GEOSPHERE

GEOSPHERE, v. 17, no. 4

https://doi.org/10.1130/GES02321.1

13 figures; 1 set of supplemental files

CORRESPONDENCE: kathie.marsaglia@csun.edu

CITATION: Johnson, K., Marsaglia, K.M., Brandl, P.A., Barth, A.P., Waldman, R., Ishizuka, O., Hamada, M., Gurnis, M., and Ruttenberg, I., 2021, Intra-oceanic submarine arc evolution recorded in an ~1-km-thick rear-arc succession of distal volcaniclastic lobe deposits: Geosphere, v. 17, no. 4, p. 957–980, https://doi.org/10.1130/GES02321.1.

Science Editor: Shanaka de Silva
Guest Associate Editor: Gray E. Bebout

Received 16 July 2020
Revision received 11 November 2020
Accepted 4 March 2021

Published online 14 May 2021

Intra-oceanic submarine arc evolution recorded in an ~1-km-thick rear-arc succession of distal volcaniclastic lobe deposits

Kyle Johnson[1], Kathleen M. Marsaglia[1], Philipp A. Brandl[2], Andrew P. Barth[3], Ryan Waldman[1], Osamu Ishizuka[4,5], Morihisa Hamada[5], Michael Gurnis[6], and Ian Ruttenberg[1]

[1]Department of Geological Sciences, California State University–Northridge, 18111 Nordhoff Street, Northridge, California 91330-8266, USA
[2]GEOMAR Helmholtz Centre for Ocean Research Kiel, Wischhofstrasse 1-3, 24148 Kiel, Germany
[3]Department of Earth Sciences, Indiana University–Purdue University, Indianapolis, Indiana 46234, USA
[4]Geological Survey of Japan/National Institute of Advanced Industrial Science and Technology (AIST), Central 7 1-1-1 Higashi, Tsukuba, Ibaraki, 305-8567, Japan
[5]Research Institute for Marine Geodynamics, Japan Agency for Marine–Earth Science and Technology, 2-15 Natsushima-cho, Yokosuka 237-0061, Japan
[6]Seismological Laboratory, California Institute of Technology, Pasadena, California 91125, USA

ABSTRACT

International Ocean Discovery Program (IODP) Expedition 351 drilled a rear-arc sedimentary succession ~50 km west of the Kyushu-Palau Ridge, an arc remnant formed by rifting during formation of the Shikoku Basin and the Izu-Bonin-Mariana arc. The ~1-km-thick Eocene to Oligocene deep-marine volcaniclastic succession recovered at Site U1438 provides a unique opportunity to study a nearly complete record of intra-oceanic arc development, from a rear-arc perspective on crust created during subduction initiation rather than supra-subduction seafloor spreading. Detailed facies analysis and definition of depositional units allow for broader stratigraphic analysis and definition of lobe elements. Patterns in gravity-flow deposit types and subunits appear to define a series of stacked lobe systems that accumulated in a rear-arc basin. The lobe subdivisions, in many cases, are a combination of a turbidite-dominated subunit and an overlying debris-flow subunit. Debris flow–rich lobe-channel sequences are grouped into four, 1.6–2 m.y. episodes, each roughly the age range of an arc volcano. Three of the episodes contain overlapping lobe facies that may have resulted from minor channel switching or input from a different source. The progressive up-section coarsening of episodes and the increasing channel-facies thicknesses within each episode suggest progressively prograding facies from a maturing magmatic arc. Submarine geomorphology of the modern Mariana arc and West Mariana Ridge provide present-day examples that can be used to interpret the morphology and evolution of the channel (or channels) that fed sediment to Site U1438, forming the sequences interpreted as depositional lobes. The abrupt change from very thick and massive debris flows to fine-grained turbidites at the unit III to unit II boundary reflects arc rifting and progressive waning of turbidity current and ash inputs. This interpretation is consistent with the geochemical record from melt inclusions and detrital zircons. Thus, Site U1438 provides a unique record of the life span of an intra-oceanic arc, from inception through maturation to its demise by intra-arc rifting and stranding of the remnant arc ridge.

Kathleen Marsaglia https://orcid.org/0000-0001-5430-4630

INTRODUCTION

The Izu-Bonin-Mariana arc system (Fig. 1) is perhaps the "type" intra-oceanic system, partly as a result of extensive Deep Sea Drilling Project (DSDP) and Ocean Drilling Program (ODP) drilling/coring that addressed major subduction-related processes, such as the origin and nature of backarc and forearc basins. Poor recovery on DSDP legs in the Mariana transect was followed by better recovery on ODP Leg 126, which provided excellent information on the nature of the Sumisu Rift and forearc basin fill, including its largely marine resedimented nature, as summarized in Marsaglia (1995). A major result of this series of ODP cruises was the realization that the magmatic history of the arc lay in the fragmented, volcaniclastic sedimentary records of forearc, intra-arc, and backarc basins as reflected in both geochemical (e.g., Gill et al., 1994; Straub et al., 2015) and petrographic (e.g., Marsaglia, 1992; Marsaglia and Devaney, 1995) data sets. These data sets complement field-based studies of accreted oceanic and continental margin arcs (e.g., Busby, 2004; Busby et al., 2006; Busby-Spera, 1985, 1988; Clift et al., 2005) and were used to interpret these terranes (e.g., Critelli et al., 2002; Marsaglia et al., 2016; Wombacher and Münker, 2000).

International Ocean Discovery Program (IODP) Expedition 351 drilling was designed to answer questions about the fundamental plate-tectonic processes of convergent margin initiation and crustal development in intra-oceanic settings by drilling at IODP Site U1438 in the 4.7-km-deep Amami Sankaku Basin located west of the Kyushu-Palau Ridge remnant arc (Fig. 1). Site U1438 provides a remarkable Eocene to Oligocene deep-marine sedimentary record of inception of the Izu-Bonin-Mariana arc and later modification by arc rifting. Continuous coring and nearly continuous recovery of a clastic section at this site allowed for detailed sedimentological analysis at the centimeter to kilometer scale (Johnson et al., 2017) and modeling of the timing and nature of input of volcaniclastic components into the basin (Barth et al., 2017; Brandl et al., 2017; Hamada et al., 2020) during the main phase of arc development in the late Eocene to early Oligocene. Prior drilling of the Izu-Bonin forearc only cored the equivalent Oligocene sedimentary record (Taylor et al., 1990). This paper relates the depositional record and stratigraphic architecture at this

site to melt evolution and crustal processes at a level of detail not attained in previous studies of intra-oceanic volcanic-arc successions (e.g., Busby et al., 2006; Clift and Lee, 1998; Clift et al., 2000, 2005; Hiscott and Gill, 1992). Our study uniquely combines detailed facies analysis with melt inclusion and detrital zircon analyses to illustrate the life span of a nascent marine arc system, including controls on the broad-scale distribution and depositional processes of volcaniclastic sediments.

GEOLOGIC SETTING

Site U1438 in the Amami Sankaku Basin lies west of the Kyushu-Palau Ridge, a remnant of the initial Izu-Bonin-Mariana arc formed following initiation of subduction, and isolated from the modern Izu-Bonin-Mariana arc at ca. 25 Ma (e.g., Ishizuka et al., 2011) by arc rifting and backarc spreading that formed the Shikoku and Parece Vela basins (Figs. 1 and 2). The 1.61-km-thick stratigraphic section at Site U1438 records the history of magmatic arc initiation and evolution from a rear-arc perspective (Arculus et al., 2015a, 2015b; Barth et al., 2017; Brandl et al., 2017; Hamada et al., 2020). We use the term "rear arc" instead of backarc for the Amami Sankaku Basin because its mafic crust did not form behind a mature arc in response to suprasubduction seafloor spreading but was created during the process of subduction initiation (Arculus et al., 2015a, 2015b). The Holocene to Eocene stratigraphy at Site U1438 was subdivided into five lithostratigraphic units (Fig. 3): Four sedimentary units (1.46 km with 76% recovery) overlying the mafic igneous basement formed soon after subduction initiation (Arculus et al., 2015b; Ishizuka et al., 2018). Sedimentary unit I is composed of postarc hemipelagic mud with minor ash beds, whereas units II and III are dominated by coarser (sand-gravel) marine volcaniclastic units, and unit IV is mixed hemipelagic and volcaniclastic sediments. The basaltic basement (unit 1) represents new oceanic crust formed by seafloor spreading during Izu-Bonin-Mariana arc initiation (Fig. 2; Hickey-Vargas et al., 2018; Ishizuka et al., 2018; Yogodzinski et al., 2018). The ~100 m interval of unit IV is thought to represent a metalliferous and hemipelagic drape over this basement, with tuffaceous laminae and coarser volcaniclastic sediments derived from local magmatism that waned prior to input from the nascent magmatic arc and accumulation of unit III prior to arc rifting and deposition of unit II (Fig. 3; Arculus et al., 2015a, 2015b; Waldman et al., 2021).

Seismic data show a wedge of presumed volcaniclastic sediment tapering away from the Kyushu-Palau Ridge to Site U1438 (Arculus et al., 2015a). The top of unit III is rather well defined as a bright reflector on both the east-west and north-south seismic lines centered on U1438 (see Supplemental Material[1]; Figs. S1, S2, and S3). The top of unit III can be traced over more than 40 km in either direction and is clearly a regional feature. However, reflectors within unit III are difficult to follow for more than 10 km, although there are several horizontal reflectors that diminish in strength with depth. About 10 km south of U1438, the reflectors become incoherent within unit III, although the top of unit III remains clear (Fig. S2). There are generally about one or two horizontal reflectors

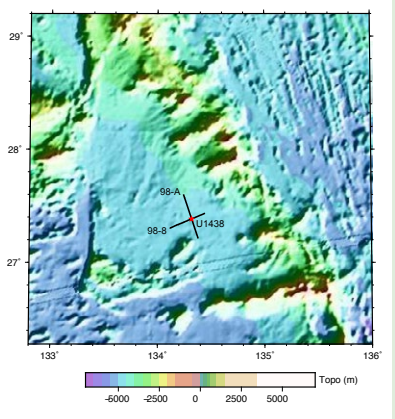

[1]Supplemental Material. Figures S1–S4. Includes seismic lines and location map for them, as well as backscatter and bathymetry data near the West Mariana Ridge analogue. Please visit https://doi.org/10.1130/GEOS.S.14167292 to access the supplemental material, and contact editing@geosociety.org with any questions.

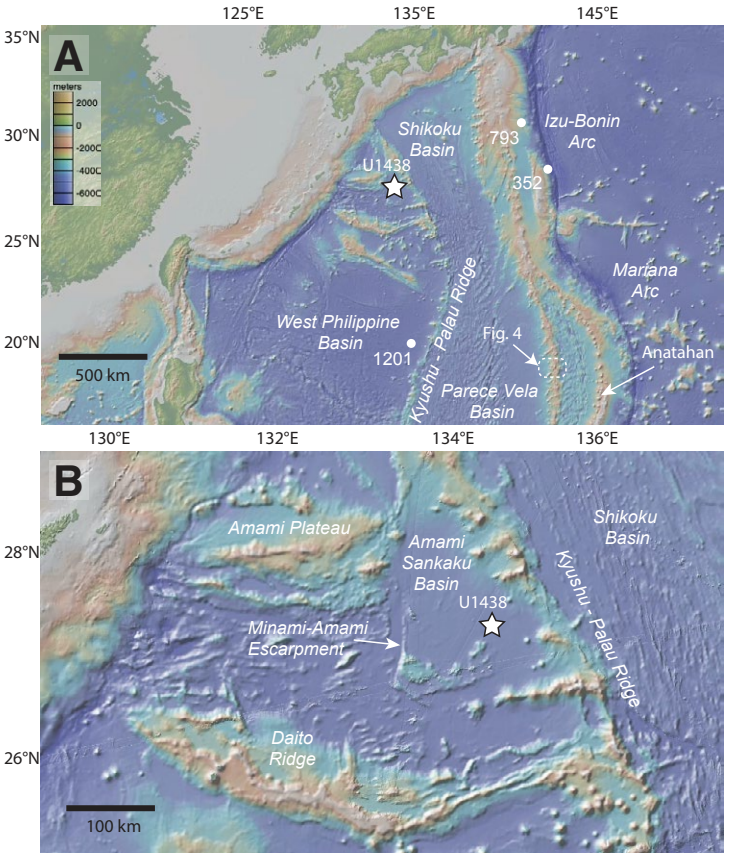

Figure 1. Bathymetric maps of the Philippine Sea region. The location of *International Ocean Discovery Program* (IODP) Site U1438 within the Amami Sankaku Basin is marked by a star. Arrow points to the location of the bathymetric image of the West Mariana Ridge segment pictured in Figure 3B.

within the middepth range of unit III, and these can be traced over ~10 km, but no further. The base of unit III is poorly defined, and unit IV and the boundary between unit IV and unit 1 are not well constrained with the seismic images because of multiple reflectors occurring within the unit III to unit 1 depth range.

Sediment ages listed in Figure 3 are based on biostratigraphic and magnetostratigraphic datums reported in Arculus et al. (2015a), with some extrapolation in the Eocene part of unit III (>800 m below seafloor [mbsf], older than 34 Ma). This model was supported by zircon maximum depositional age (MDA) increasing from 29 to 37 Ma from 350 to 1000 mbsf (Barth et al., 2017) and by a new 39–47 Ma age model for unit IV (Waldman et al., 2021). Sediment accumulation rates decreased from ~120 m/m.y. in units II and III

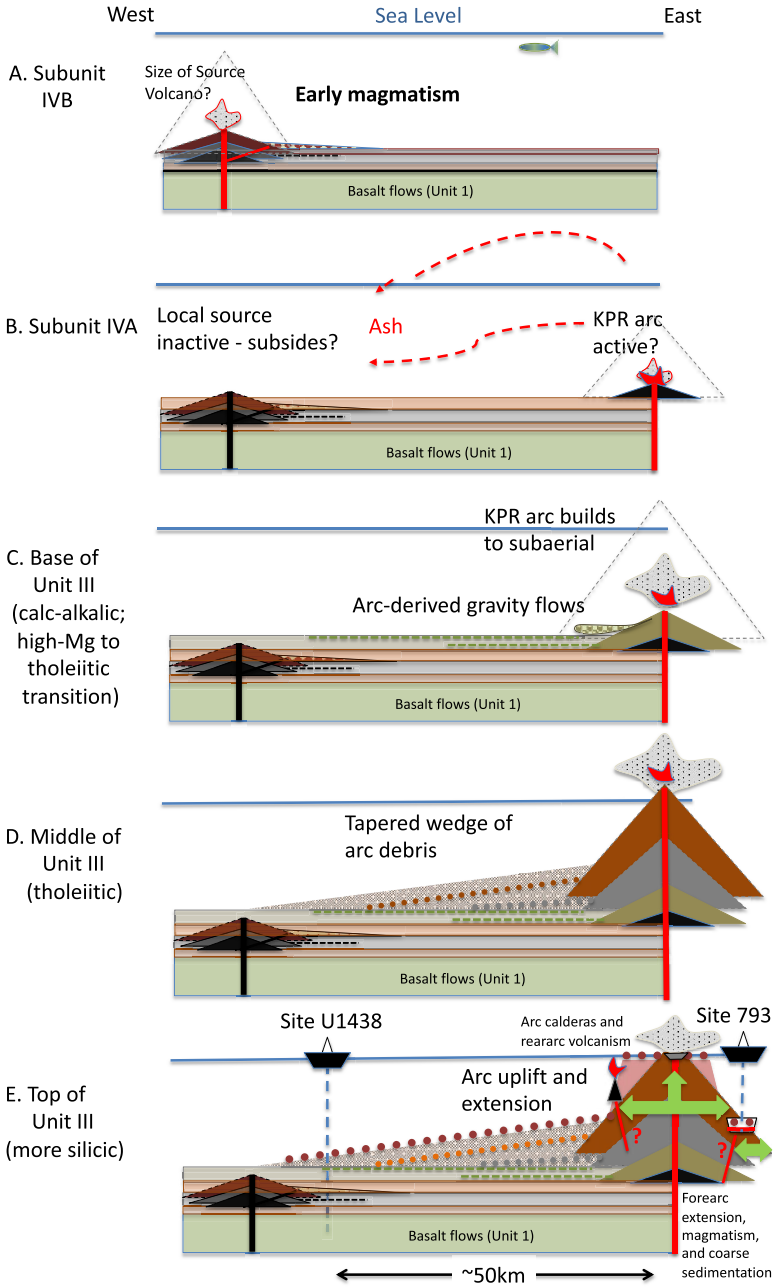

Figure 2. (A–E) Series of cartoon diagrams modified from Waldman et al. (2021) to include middle and upper sections of unit III at Site U1438 and further evolution of the Kyushu-Palau Ridge arc to the east. They summarize sedimentological and facies observations and interpretations above the basalt flows of igneous unit 1, starting with lithostratigraphic unit IV and progressing up through unit III. Vertical and horizontal scales have been modified. In E, deep-ocean drilling is depicted by the drill ships at *International Ocean Discovery Program* (IODP) Site U1438 and Ocean Drilling Program (ODP) Site 793. The dashed profiles over volcanoes show potential maximum size variation of volcanic edifices in A, B, and C. (A) Basalt flows formed during early spreading and magmatism (unit 1) and overlying ca. 47 Ma mudstones (subunit IVC) form the foundation upon which a volcanic center developed with a volcanic apron built of shallow water–derived volcaniclastic turbidites (subunit IVB) intruded by magma (see Arculus et al., 2015b; Waldman et al., 2020). (B) Local volcanic quiescence and first potential input of ash to the rear-arc mudstone (subunit IVA), heralding the development of the Kyushu-Palau Ridge (KPR) magmatic arc to the east. (C) Further arc edifice development and input of arc-derived gravity flows to the drill site with calc-alkalic volcanic components transitioning from high-Mg to tholeiitic in composition (basal unit III). (D) Development of a wedge of more tholeiitic volcaniclastic sediment extending from the maturing Kyushu-Palau Ridge westward into the rear arc (middle unit III). (E) Extension and uplift (large green arrows) of Kyushu-Palau Ridge produce coarse clastic material, which is shed simultaneously into the rear arc (Site U1438) and into an extensional (small green arrows) forearc basin floored by basalt (Site 793). Extension-related silicic magmatism and likely caldera formation along the arc are accompanied by development of rear-arc volcanic centers, which also feed clasts to the rear-arc wedge. Extension ultimately progresses to rifting (unit II tuffaceous deposits at Site U1438) and seafloor spreading, forming the Shikoku Basin (Fig. 1).

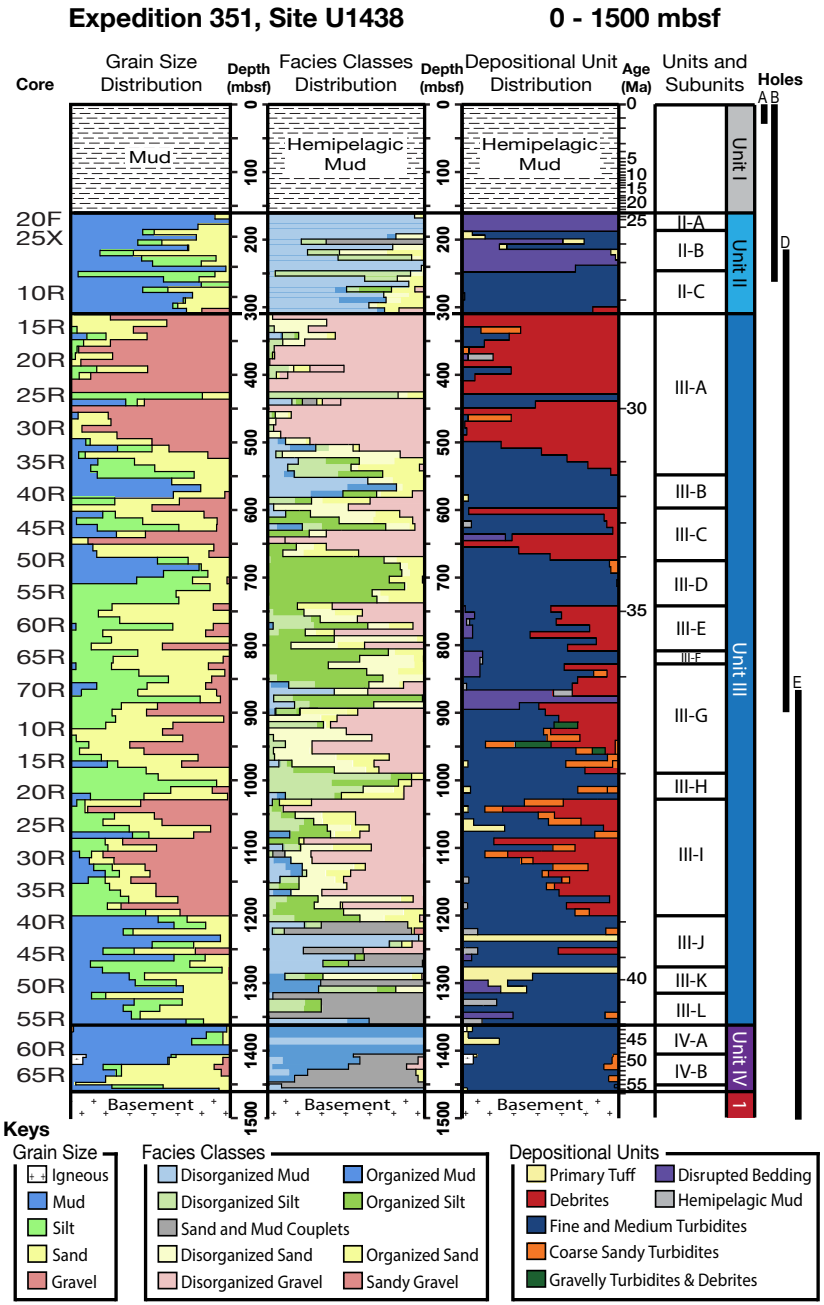

Figure 3. Downhole distributions of grain size, facies classes, and depositional units, on a core-by-core basis (mbsf—meters below seafloor). Subunits of unit III outlined in this study are defined to the right, along with shipboard-defined units and ages (Arculus et al., 2015a). Bin size is one 9.5 m core interval (9.5 m or less recovery). See Johnson et al. (2017) for database and more information on classification schemes.

(Eocene to Oligocene) to ~5 m/m.y. in unit I (Miocene to Holocene) after arc rifting progressed to seafloor spreading in the Shikoku Basin.

Unit III at Site U1438 thus records the development of a segment (central Kyushu-Palau Ridge) of the submarine Izu-Bonin-Mariana arc (e.g., Brandl et al., 2017; Fig. 2). In this study, we summarized the nature of the coarse volcaniclastic marine depositional units, interpreted their depositional processes, and identified trends and recognized subunits. The nature and sequence of subunits allowed us to create a model for distal deep-marine rear-arc basin sedimentation that was then integrated with geochemical data from igneous detritus. This model can be applied to other intra-oceanic backarc/rear-arc successions, such as those recovered at Ocean Drilling Program (ODP) Site 1201 (Shipboard Scientific Party, 2002) and perhaps to more proximal arc facies, such as those that crop out in Baja California (Busby et al., 2006; Critelli et al., 2002).

METHODS

Grain size, sedimentary structures, bioturbation, bedding characteristics, facies, and depositional unit classification data are reported for each core in Johnson et al. (2017) (Fig. 3). Sedimentary facies were classified using the scheme outlined in Pickering et al. (1986) and Pickering and Hiscott (2015): A (gravel), B (sand), C (sand/mud couplet), D (silt), and E (clay), with further group subdivision and indication of degree of organization. Depositional unit types associated with gravity flows (e.g., turbidite, sandy/muddy debris flow) were also identified. Some more massive, fine-grained (tuffaceous mudstone) beds with sharp contacts showed no apparent internal grading or scoured bases. These were considered to be of pyroclastic origin and classified as tuff according to criteria set forth by shipboard scientists, whose analysis included smear-slide and thin-section observations of dominantly vitric components in unit III examples (see discussion in Arculus et al., 2015a). Turbidite subdivisions were designated using subdivisions of Lowe (1982; coarse grained), Bouma (1962; medium grained), and Stow and Shanmugam (1980; fine grained). Other categories were devised for debris flow, mud/mudstone, and tuff/lapillistone units. These data, presented in Johnson et al. (2017), were interpreted here using the pattern of lobe depositional unit types and proportions to interpret arc evolution.

First, 100-m-scale stratigraphic summaries were constructed by graphically illustrating changes in gravity-flow depositional unit type: fine-grained turbidites (no Bouma Ta or Tb divisions present), medium-grained turbidites (Bouma Tb division present but no Ta division), coarse-grained turbidites (Bouma Ta and/or any Lowe divisions present), and debrites (debris-flow deposits). Each depositional unit was assigned a specific grayscale color, where progressively darker gray indicated coarser-grained depositional unit types. Patterns within the stratigraphic columns and the depositional unit distribution were correlated to submarine channel and lobe facies described by Mutti and Normark (1987) and fan models as summarized by Covault (2011). Twelve potential lobe systems were identified, based on lobe and channel facies criteria introduced by Mutti and Normark (1987). The base of each lobe system was defined as an interval of mud-rich lobe-fringe or distal lobe facies. Distal facies are generally overlain by intermediate to proximal lobe-axis facies, which are defined by increasing proportion of interbedded debrites. Channel facies are debrite-dominated features and contain a fining-upward top. These definitions are consistent with more recent 2- to 3-dimensional outcrop- and seismic-based studies of lobe systems and complexes (e.g., Prélat et al., 2009; Pyles et al., 2019; Sweet et al., 2020), which further develop the architectural hierarchy from the bed to the lobe to the lobe system scale within a lobe complex. Within such lobe systems and complexes, lobes may stack vertically or laterally migrate (autocyclic switching) and overlap, constructing thick fan successions (see previously cited publications for details).

Petrographic thin sections were created from 166 samples from unit III. Prior to thin-section preparation, billets were first impregnated with blue epoxy for porosity recognition. Thin sections were reviewed for general composition and texture. Selected thin sections were stained to aid with determination of feldspar and zeolite mineralogy using the techniques of Marsaglia and Tazaki (1992) and then point-counted for primary grain types, authigenic phases, and porosity.

RESULTS

Facies, Depositional Units, and Lobes

This work builds on the preliminary results presented in Johnson et al. (2017), which we first briefly summarize here. Downhole distributions of grain sizes, facies classes, and depositional unit types are displayed in Figure 3, where percentages are shown in histogram fashion with each bar representing one core (~9.5 m interval). The patterns of facies classes are roughly affiliated with certain grain sizes, and therefore these two attributes exhibit very similar downhole patterns. Generally, turbidites correlate with mudstone (facies class E), siltstone (facies class D), and sandstone (facies classes B and C), and debrites correlate with gravelly sandstone (facies class A1.4) and conglomerate (facies class A1.1). There are some exceptions to this correlation. For example, debrites may also contain facies class B sandstone in fine-grained intervals. Patterns in the distribution of depositional unit types were used to separate unit III into 12 subunits (Johnson et al., 2017). These subunits generally alternate between debrite-poor and debrite-rich intervals. The overall percentages of each bed type in unit III are as follows: ~57% turbidites (fine- and medium-grained), ~31% debrites, ~3% coarse-grained turbidites, ~2% tuff/lapillistone, and ~1% structureless mud deposits.

If we interpret these beds to be gravity-flow deposits supplied by submarine channels emanating from the arc axis 50 km to the east (Kyushu-Palau Ridge [KPR], remnant arc; Fig. 1), we can interpret the succession using depositional lobe models developed for submarine channel-fan complexes, which would form the seismically defined wedge of presumed volcanogenic materials that extends from the Kyushu-Palau Ridge to the drill site. Given our limited 1-dimensional view from a single drill site, we chose to simplify our model (Fig. 4A), where the facies are defined as: channel, transitional channel-lobe,

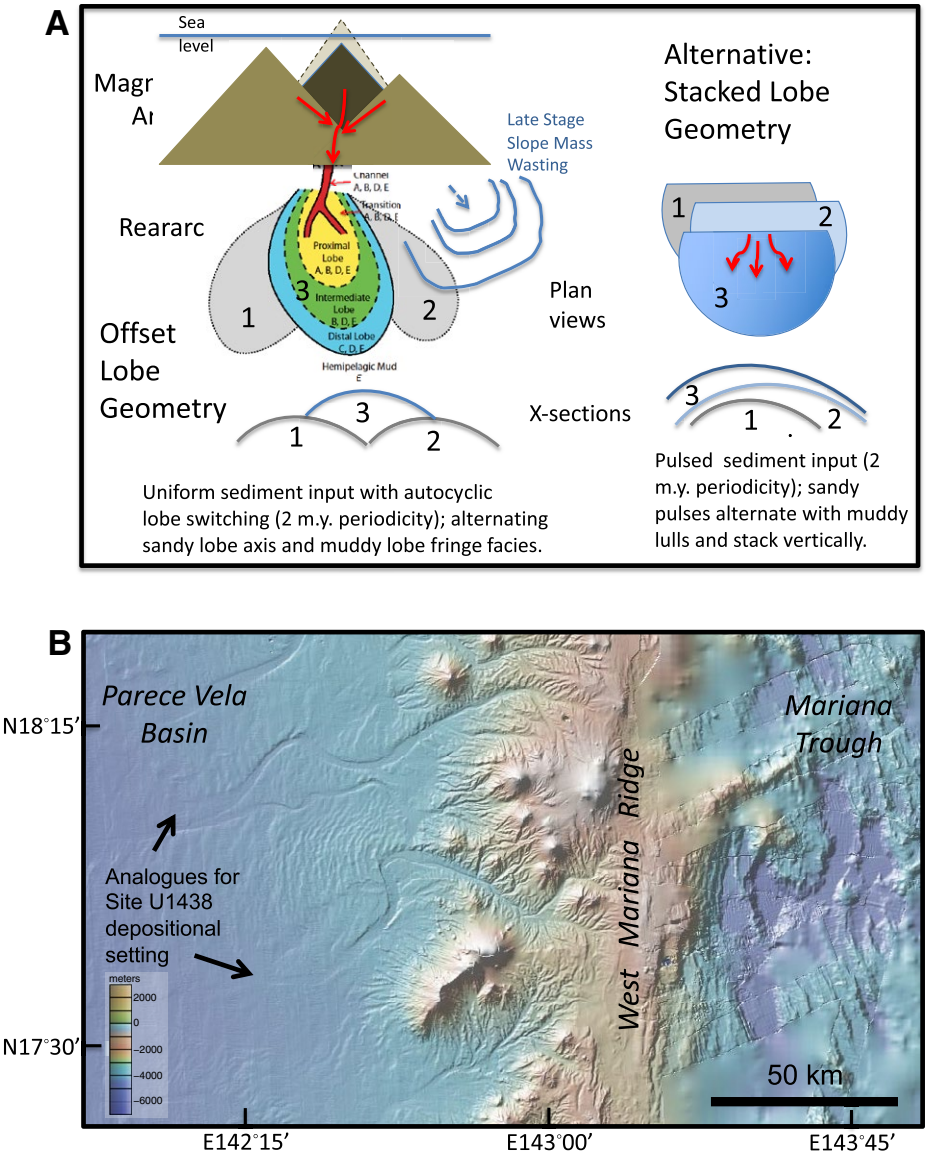

Figure 4. (A) Schematic diagram model for channel-feeder system (red) and depositional lobes extending from the Kyushu-Palau Ridge into the rear arc. Center shows a schematic model for the distribution of lobe facies based on descriptions by Mutti and Normark (1987) with possible lobe switching depicted. Letters are Pickering and Hiscott (1986) facies classes affiliated with each lobe facies. An alternate lobe configuration is pictured on the left, and mass-flow deformation is pictured on the right. (B) Bathymetric image of the West Mariana Ridge created in October 2020 with GeomapApp from data provided by Scripps Institution of Oceanography (*SIO*), National Oceanic and Atmospheric Administration (NOAA), U.S. Navy, Global Multi-Resolution Topography in GeoMapApp, and General Bathymetric Chart of the Oceans (GEBCO). Also see Ryan et al., 2009.

proximal lobe, intermediate lobe, or distal lobe (lobe-fringe). Individual debrite and turbidite beds stack to form a lobe, and lobes stack vertically or offset to form a lobe system (Fig. 4A). The hemipelagic mud and fine-grained turbidite deposits are stratigraphically significant in that they were used to subdivide the succession into lobe systems starting at the base of unit III.

Lobe system 1 (Fig. 5) spans from subunit III-L to III-I and is 184 m thick. Subunit III-L is distinguished by its very thin, fine-, medium-, and coarse-grained turbidites and muddy beds. The turbidites are classified as lobe-fringe deposits, and the muddy deposits are classified as hemipelagites. Tuff bed proportion increases through subunit K starting in core U1438E-50R (~1310 mbsf), where tuff is 17% of the core, and dissipates above core U1438E-47R (~1285 mbsf), where tuff is 100% of the core. These tuff beds are separated by disturbed fine- and medium-grained turbidites, thicker than those in subunit III-L. Throughout the system, depositional unit thicknesses and grain sizes gradually increase in a coarsening-upward succession that transitions to proximal lobe deposits at the top of subunit III-J.

The 15.5-m-thick lobe system 2 (Fig. 6) begins within subunit III-I and is the second-thinnest lobe of unit III. The sequence begins in core U1438E-36R (~1180 mbsf) with intermediate lobe deposits capping the coarse transitional facies that top lobe system 1. A transition from fine-grained turbidites to coarse-grained turbidites to debrites spans the top half of core U1438E-36R and the bottom half of core U1438E-35R (~1175 mbsf) before a sharp drop in grain size occurs at the top of the lobe.

At 76 m thick, lobe system 3 (Fig. 6) spans from core U1438E-35R to core U1438E-27R (~1090 mbsf). There is a 7 m buildup from distal lobe facies to transitional facies extending through the top ~60 m of the system where channel facies occur. Within the transitional facies, two intervals of proximal lobe facies occur.

Lobe system 4 (Fig. 6) spans 57 m from core U1438E-27R to the top of subunit III-I in core U1438E-20R (~1025 mbsf). The sequence transitions into intermediate and proximal lobe deposits. Distal facies transition to channel deposits until core U1438E-22R (~1045 mbsf), above which channel deposits dominate.

Lobe system 5 (Fig. 7) begins at the base of fine-grained turbidite-rich subunit III-H, which is made up completely of lobe-fringe facies. The top of the subunit, core U1438E-16R (~985 mbsf), contains intermediate lobe facies that

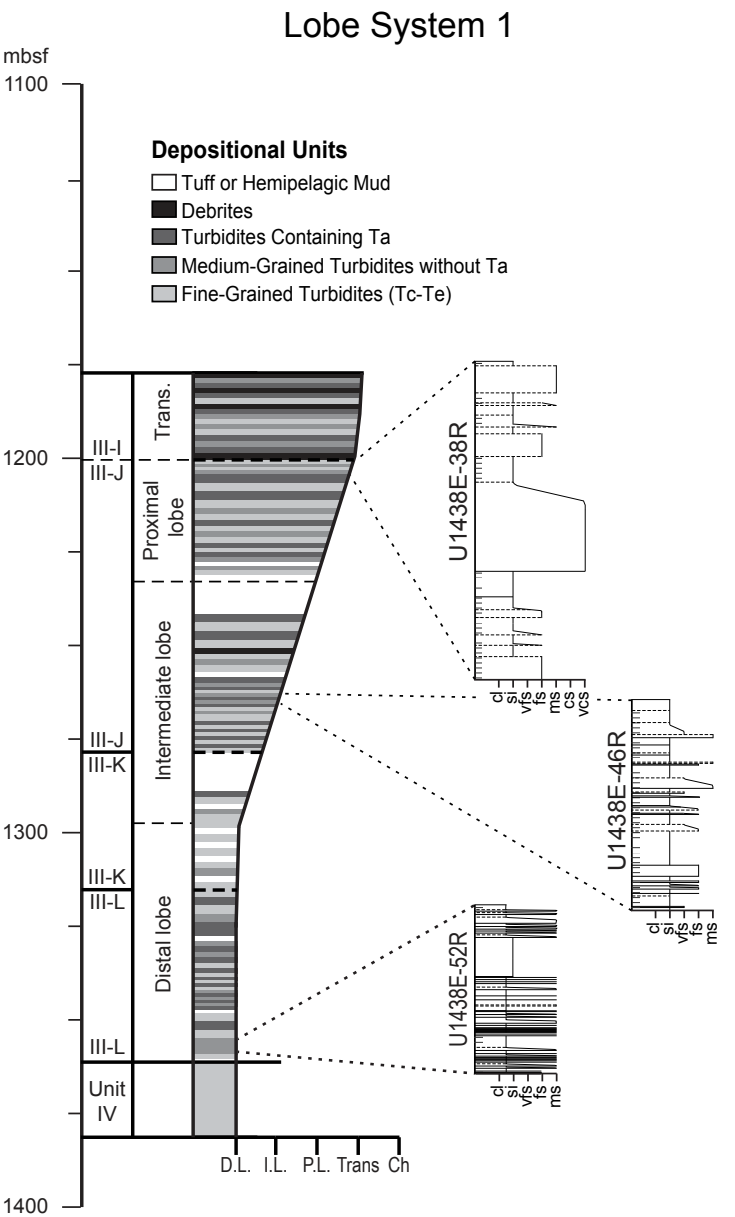

Figure 5. Details of lobe system 1, which is interpreted as the first buildup of the arc edifice following arc initiation. The darker colors correspond with intervals of coarser material, where debrites are black and fine-grained turbidites are the lightest gray. White intervals are tephra or hemipelagic mud. Width of the column in this visualization corresponds to facies outlined in Figure 3: distal lobe (D.L.), intermediate lobe (I.L.), proximal lobe (P.L.), channel-lobe transition (Trans.), and channel (Ch.) facies, where distal lobe facies are narrow intervals, and the widest portions of the column are channel facies. Subunits are labeled within column; mbsf—meters below seafloor. cl—clay, si—silt, vfs—very fine sand, fs—fine sand, ms—medium sand, cs—coarse sand, vcs—very coarse sand, gr—gravel. See Supplemental Material for core summary column details (text footnote 1).

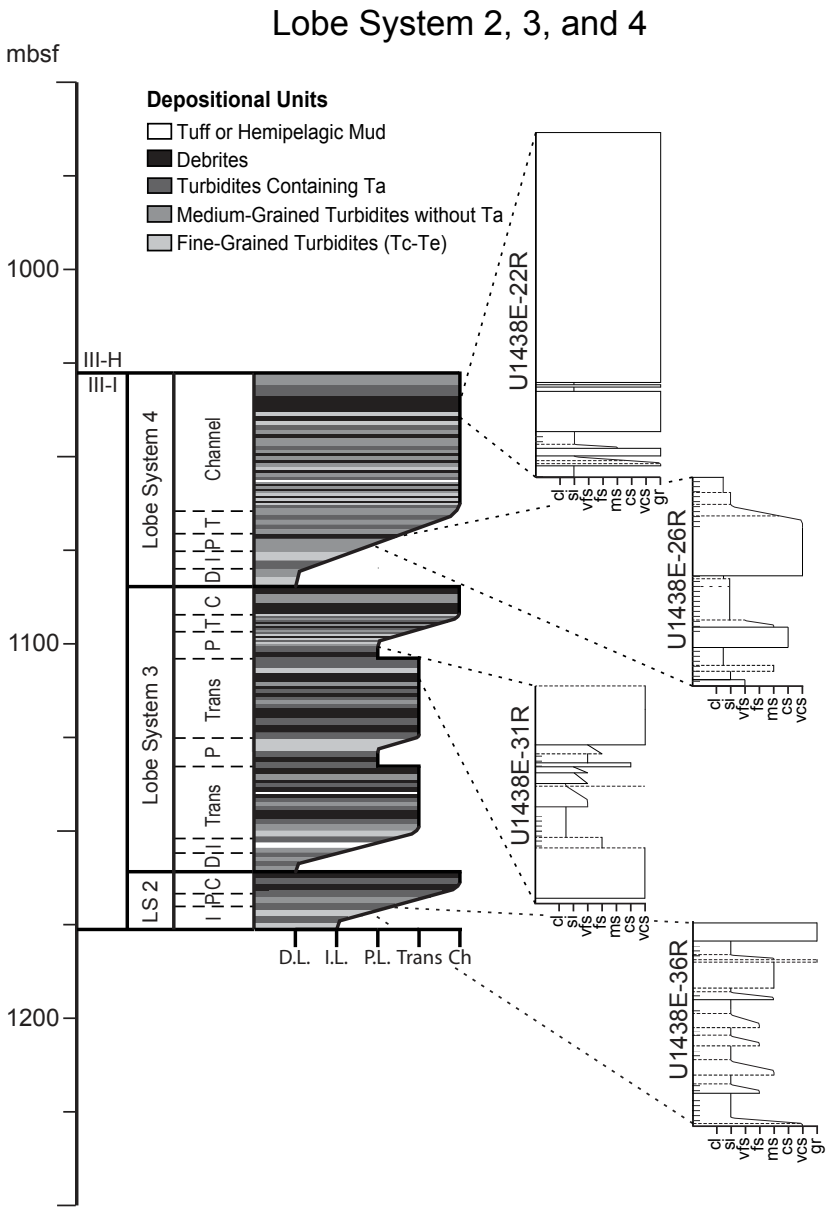

Figure 6. Details of lobe systems (LS) 2–4, which were deposited during the first edifice-failure episode. The darker colors correspond with intervals of coarser material, where debrites are black, and fine-grained turbidites are the lightest gray. White intervals are tephra or hemipelagic mud. Width of the column in this visualization corresponds to facies outlined in Figure 5: distal lobe (D.L. or D), intermediate lobe (I.L. or I), proximal lobe (P.L. or P), channel-lobe transition (Trans or T), and channel (Ch or C) facies, where distal lobe facies are narrow intervals, and the widest portions of the column are channel facies. Subunits are labeled within column; mbsf—meters below seafloor. cl—clay, si—silt, vfs—very fine sand, fs—fine sand, ms—medium sand, cs—coarse sand, vcs—very coarse sand, gr—gravel. See Supplemental Material for core summary column details (text footnote 1).

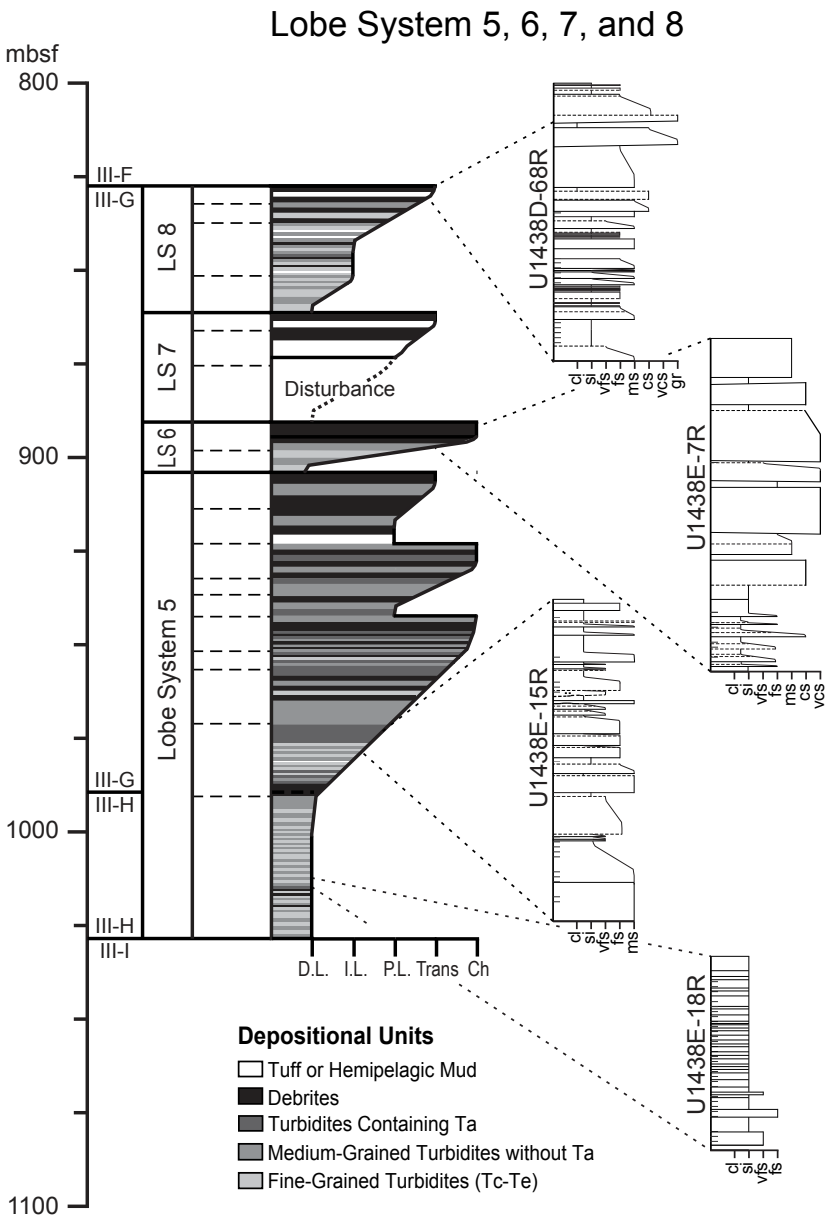

Figure 7. Details of lobe systems (LS) 5–8, which define a second major edifice-failure episode. The darker colors correspond with intervals of coarser material, where debrites are black, and fine-grained turbidites are the lightest gray. White intervals are tephra or hemipelagic mud. Width of the column in this visualization corresponds to facies outlined in Figure 5: distal lobe (D.L. or D), intermediate lobe (I.L. or I), proximal lobe (P.L. or P), channel-lobe transition (Trans or T), and channel (Ch or C) facies, where distal lobe facies are narrow intervals, and the widest portions of the column are channel facies. Subunits are labeled within column; mbsf—meters below seafloor. cl—clay, si—silt, vfs—very fine sand, fs—fine sand, ms—medium sand, cs—coarse sand, vcs—very coarse sand, gr—gravel. See Supplemental Material for core summary column details (text footnote 1).

grade upward into proximal, transitional, and then finally channel facies in core U1438E-12R (~950 mbsf). The top of core U1438E-12R, however, contains proximal lobe facies that coarsen upward into channel deposits. This occurs again in core U1438E-9R (~920 mbsf), grading from proximal to transitional facies as the 124-m-thick lobe system terminates.

The 13.4-m-thick lobe system 6 (Fig. 7) is the thinnest of all identified systems deposited at Site U1438. Between cores U1438E-8R (~910 mbsf) and U1438E-7R (~900 mbsf), facies transition from distal lobe to channel. The lobe is roughly defined using grain size within a highly disturbed zone (drilling and/or soft-sediment deformation) at the Hole E/Hole D overlap zone between core U1438D-72R (~890 mbsf) and core U1438E-7R (~900 mbsf).

Lobe system 7 (Fig. 7) begins in a highly disturbed zone from the top of core U1438D-72R (~890 mbsf) to the top of core U1438D-70R (~870 mbsf), at the bottom of drilled Hole D, with a total thickness of ~20.7 m. The disturbed sediment appears to be fine grained, so it is assumed to be the distal facies of a lobe system and separate from the coarse material of lobe system 6 directly below. Overlying the disturbed sediment are proximal lobe and channel-lobe transition facies that fine upward into the overlying lobe system 8. Shipboard scientists (Arculus et al., 2015a) interpreted the disrupted zone as a product of normal faulting, so there may be missing section in this interval.

A thick sequence of very thinly bedded turbidites makes up the majority of lobe system 8 (Fig. 8), which has a thickness of 33.8 m. An increasing content of interbedded coarse-grained intervals constitutes a coarsening-upward transition of lobe facies. The thin-bedded intervals continue into channel-lobe transitional facies at the top of the sequence and then fine upward into the overlying lobe system 9.

Lobe system 9 (Fig. 8) spans from subunit III-F to III-E (86 m). Subunit III-F contains proximal to intermediate lobe deposits, where alternating medium- to coarse-grained turbidites and fine-grained turbidites form thin packages. Periodic thick (0.5–1 m) coarse turbidites are intermediate lobe facies. The overlying subunit III-E consists of channel-lobe transition facies. Above the subunit III-E to III-F boundary, facies transition upward to intermediate lobe facies, for a short interval and then coarsen upward to channel facies. Following a thin channel-facies interval, intermediate facies return before another facies sequence that terminates with channel-lobe transitional facies.

Lobe system 10 (Fig. 8) spans from subunit III-D to III-C (106 m thick). Subunit III-D is made up of distal lobe-fringe facies that transition to intermediate lobe facies at the top. The bottom of subunit III-C continues the thick facies transition started in III-D. In cores U1438D-46R (~640 mbsf), U1438D-47R (~650 mbsf), and U1438D-48R (~660 mbsf), thick channel facies debrites mark the top of the lobe system.

Lobe system 11 (Fig. 8) is the second lobe that occurs within subunit III-C and is much thinner (39 m vs. 106 m). Above the thick debrites of lobe system 10, distal, intermediate, and proximal lobe facies mark the base of lobe system 11. In core U1438D-44R (~620 mbsf), debrites mark the introduction of channel facies that terminate in core U1438D-42R (~600 mbsf). A short fining-upward sequence leads into subunit III-B.

As the thickest (288 m) and most complex system deposited at Site U1438, lobe system 12 (Fig. 9) consists of subunits III-A and III-B. The base (subunit III-B) contains intermediate to distal lobe facies with alternating medium-grained turbidites and disturbed fine-grained turbidites with few coarse turbidites and tuff beds. These pass upward into intermediate lobe facies and then to proximal lobe facies (core U1438D-34R, ~520 mbsf), and then channel facies beginning at core U1438D-33R. The top of core U1438D-33R (~510 mbsf) and the bottom of core U1438D-32R (~505 mbsf) contain thin and fine turbidites that lack Ta divisions, a characteristic of intermediate lobe facies. The top of core U1438D-32R contains proximal lobe facies that grade up into channel facies by core U1438D-31R (~495 mbsf). A thin interval of distal lobe facies (core U1438D-25R, ~435 mbsf) is abruptly overlain in core U1438D-24R (~425 mbsf) by thick debrites. Four meters of section were not recovered between core U1438D-25R and U1438D-24R, so the nature of the exact facies transition is unknown. Channelized debrites continue until core U1438D-16R (~350 mbsf), which contains thin turbidite and debrite interbeds. Core U1438D-16R displays a short transitional interval with channel facies debrites, overlain by an interval of thick debrites without turbidites. Given the massive debrites above and below the distal lobe facies, the sediment package was treated as one lobe system.

These lobe systems are summarized in Figure 10. This column shows the distribution of lobes and changes in their nature up through unit III.

Petrographic Data and Observations

Our petrographic observations are consistent with the shipboard core and thin-section descriptions of sandy to breccia/conglomeratic facies, showing that they are mostly clast supported and polymictic with clasts of pumice, a variety of volcanic rock fragments (lithic clasts), and rare scoria. In general, tuffaceous sandstone samples contain ~10%–20% crystals. Downhole, zeolite and clay mineral grain replacements and cements become pervasive. These are illustrated in Figure 11.

Point-count data for eight of the least-altered samples in the upper few hundred meters of unit III (320–494 mbsf) show them to contain mainly volcanic lithic fragments (average 69%), with lesser feldspar (average 24%) and mafic dense minerals (average 7%), as pictured in Figure 11. The proportions of vitric to microlitic to lathwork volcanic-lithic textures average 7:39:54, respectively, and the proportions of glassy volcanic (Lvv, Lvml, Lvl) fragments with colorless (felsic composition), brown (intermediate to mafic composition), and black (mafic composition) groundmasses average 5:61:34, respectively (for discussions of glass color and composition, see Marsaglia, 1992, 1993). Although these samples were the "least altered," they still contained, on average, 20% authigenic clay and 12% authigenic zeolites as pore-filling cements and grain replacements. Those authigenic phase percentages significantly increase with additional burial below 500 mbsf to a point where there is little left of the original glass and mineralogy. Alteration takes the form of direct

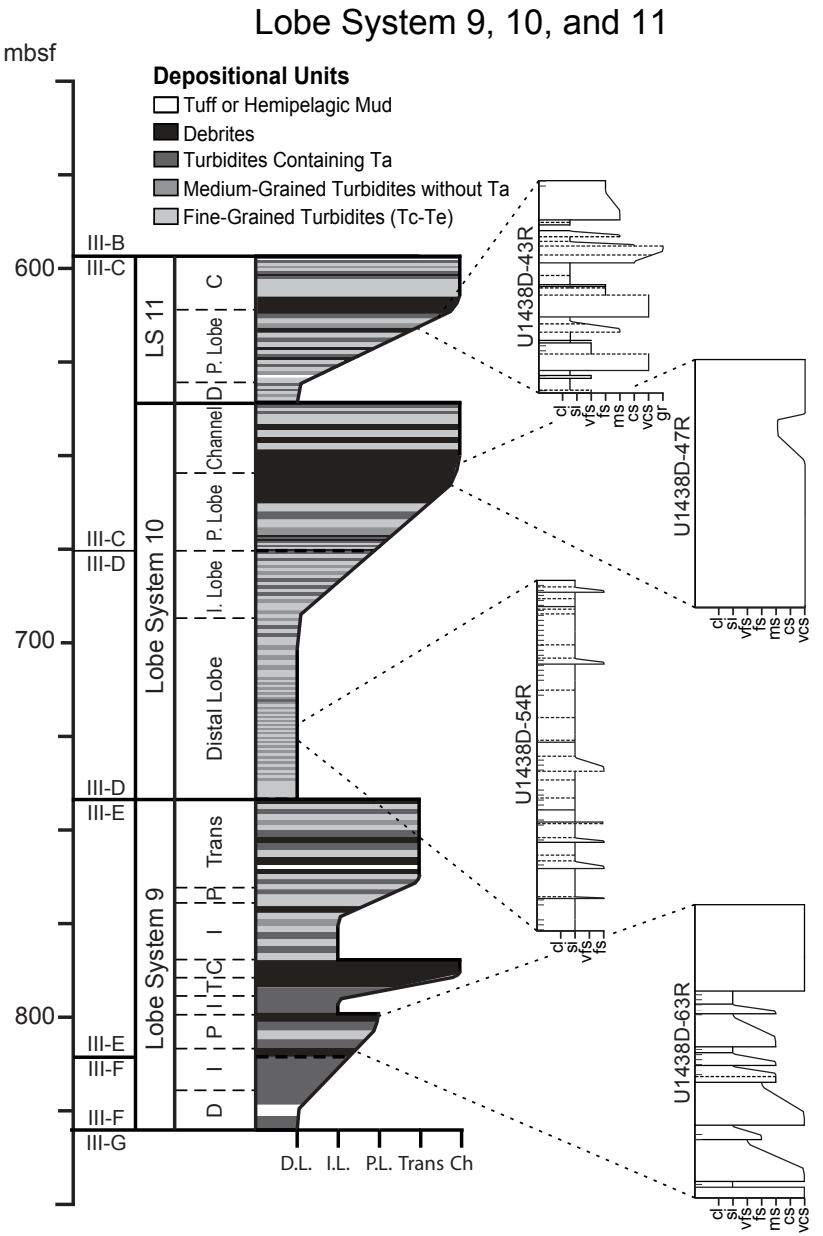

Figure 8. Detailed look at lobe systems (LS) 9–11, which define the second and third edifice-failure episodes; these are separated by the ~50 m distal lobe interval in subunit III-D. The darker colors correspond with intervals of coarser material, where debrites are black, and fine-grained turbidites are the lightest gray. White intervals are tephra or hemipelagic mud. Width of the column in this visualization corresponds to facies outlined in Figure 5: distal lobe (D.L. or D), intermediate lobe (I.L. or I), proximal lobe (P.L. or P), channel-lobe transition (Trans or T), and channel (Ch or C) facies, where distal lobe facies are narrow intervals, and the widest portions of the column are channel facies. Subunits are labeled within column; mbsf—meters below seafloor. cl—clay, si—silt, vfs—very fine sand, fs—fine sand, ms—medium sand, cs—coarse sand, vcs—very coarse sand, gr—gravel. See Supplemental Material for core summary column details (text footnote 1).

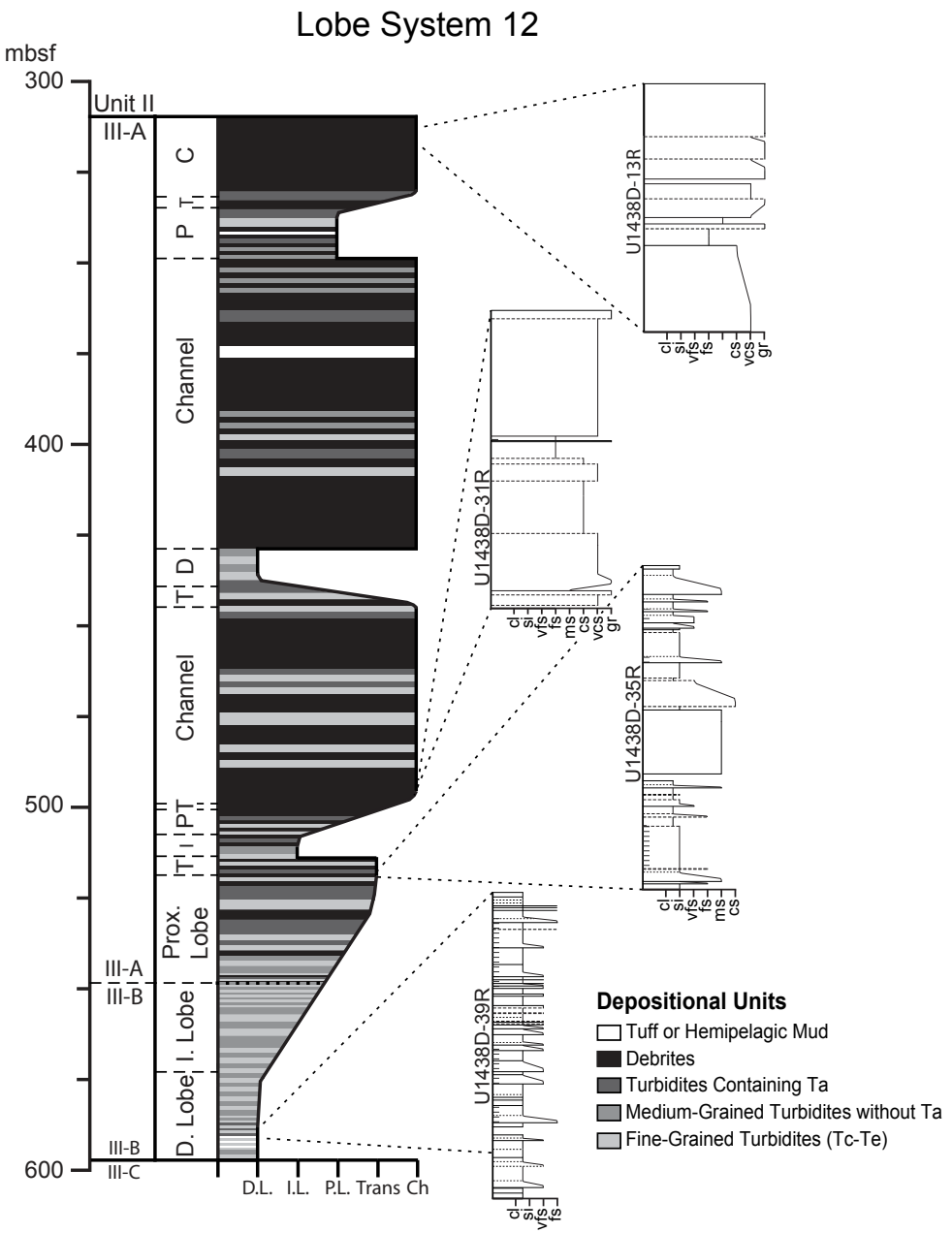

Figure 9. Detailed look at lobe system 12, which is the last episode before arc rifting thought to have begun at the unit III to unit II boundary at the top of the system. The darker colors correspond with intervals of coarser material, where debrites are black, and fine-grained turbidites are the lightest gray. White intervals are tephra or hemipelagic mud. Width of the column in this visualization corresponds to facies outlined in Figure 5: distal lobe (D.L. or D), intermediate lobe (I.L. or I), proximal lobe (P.L. or P), channel-lobe transition (Trans or T), and channel (Ch or C) facies, where distal lobe facies are narrow intervals, and the widest portions of the column are channel facies. Subunits are labeled within column; mbsf—meters below seafloor. See Supplemental Material for core summary column details (text footnote 1). cl—clay, si—silt, vfs—very fine sand, fs—fine sand, ms—medium sand, cs—coarse sand, vcs—very coarse sand, gr—gravel.

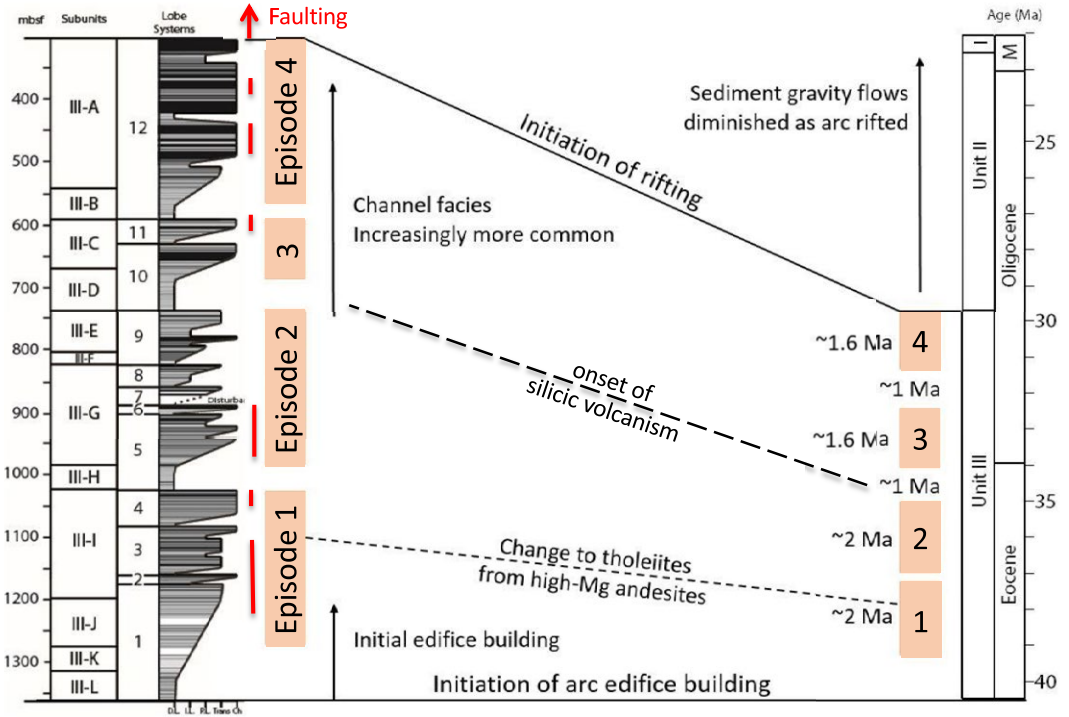

Figure 10. Overview of the distribution of identified unit III channel-lobe systems and their correlated facies and subunits. The darker colors correspond with intervals of coarser material, where debrites are black, and fine-grained turbidites are the lightest gray. White intervals are tuff or hemipelagic mudstone. Width of column in this visualization corresponds to facies outlined in Johnson et al. (2017): distal lobe (D.L.), intermediate lobe (I.L.), proximal lobe (P.L.), channel-lobe transition (Trans.), and channel facies (Ch.), where distal lobe facies are narrow, and the widest portions of the column are channel facies; mbsf—meters below seafloor. Each lobe system is detailed further in Figures 5–9. Intervals marked in red are intervals where dipping beds imply some structural deformation based on shipboard core description (Arculus et al., 2015a). The Site U1438 time scale based on Arculus et al. (2015a), Brandl et al. (2017), and Barth et al. (2017) is shown in the right side; M—Miocene.

replacement of glass (devitrification) by clay minerals, or more often dissolution of glass and replacement by authigenic clay minerals and zeolites. Plagioclase feldspar and mafic dense minerals have also been dissolved and replaced. Luckily, this alteration process preserved the volcanic lithic internal texture (e.g., vitric, microlitic, and lathwork) and phenocryst attributes (cleavage, crystal shape, zoning) that allow for the broad classification of the sampled intervals (Fig. 11).

The best-preserved volcanic lithic fragments are those composed of black opaque-rich tachylitic glass (Fig. 11) produced during subaerial mafic magmatism (Fisher and Schmincke, 1984; Carey et al., 1998). Many samples classified as largely microcrystalline contained tachylitic fragments (e.g., point-counted samples above), but there were only four tachylite-rich samples (622, 348, 911, and 1019 mbsf). An additional concentration of palagonite-rich mafic volcaniclastic samples was present from 631 to 679 mbsf (5 samples).

Approximately 11% of the samples (n = 19) exhibited rounded to subrounded grains (Fig. 11), and these were dominantly microcrystalline varieties (n = 17), with a few more vitric-rich varieties. They sporadically occurred throughout the sections down to 1000 mbsf (329, 331, 332, 348, 378, 590, 622, 631, 725, 768, 781, 804, 826, 846, 854, 869, 883, 904, and 1000 mbsf). Notably, none was observed in unit III below 1000 mbsf. Other samples stood out because they contained carbonate bioclasts and/or debris (380, 388, and 610 mbsf); all three were from samples classified as "mixed." Two vitric intervals contained largely blocky shards (824 and 1349 mbsf), and two "mixed" turbidites contained plutonic fragments (737 and 1083 mbsf).

All of the sand-bearing thin sections were reviewed and classified as to the proportion of purely vitric versus microcrystalline (microlitic/lathwork) volcanic components that they contained, comprising two end-member groups and a transitional group: 28 dominantly vitric, 100 dominantly microlitic/lathwork, and 17 with intermediate (vitric-microcrystalline) proportions. The remaining thin sections were from intervals too altered or too fine grained to verify component morphologies; these were often classified as disrupted intervals, tuff, or fine-grained turbidites based on macroscopic attributes of the core. We found no correlation between bed type and volcanic sandstone componentry, with vitric and microcrystalline group samples coming from a broad range of turbidite and debrite bed types, and with a few vitric-dominated samples from beds classified as tuff. Each of the point-counted samples was classified as microcrystalline dominated prior to selection for counting, and they came from a wide variety of turbidite and debrite types.

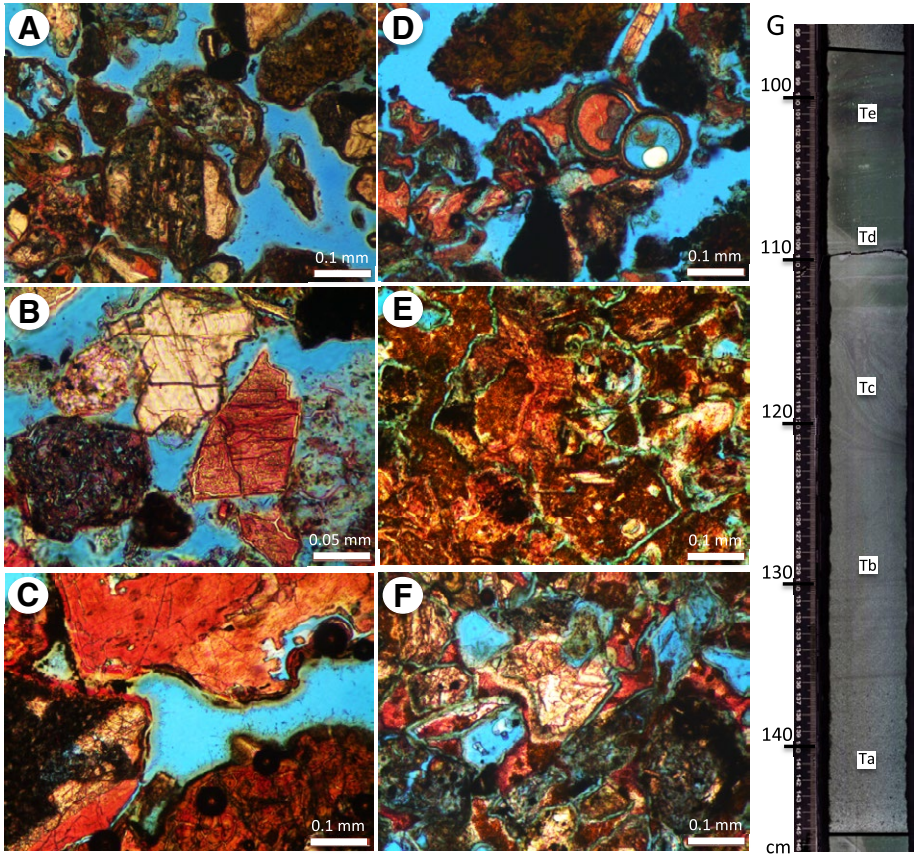

Figure 11. Photomicrographs (A–F) and core (G) images from Site U1438. Note that all microscope images (A–F) are under plane-polarized light, as they generally exhibit little birefringence when polars are crossed. All thin sections were impregnated with blue epoxy for porosity recognition (both primary and secondary) and stained for feldspar recognition. This resulted in light pink stain/etch of plagioclase feldspar and dark pink staining of Ca-rich zeolite. Authigenic clay cements range from green to brown. (A) Sample U1438D-13R-4–24 (~320 m below seafloor [mbsf]): Sandstone composed of variably altered, subangular to rounded volcanic lithic fragments exhibiting microlitic to lathwork textures. Interparticle porosity (blue) is locally filled by red-stained Ca-zeolite on left. Brown to greenish coatings on grains are clay-rim cements. (B) Sample U1438D-16R-2–52 (~350 mbsf): Carbonate grain (replacement?) in upper center, and variably altered opaque-rich volcanic grains, with microporous volcanic glass altered to clay and red-stained Ca-rich zeolite. (C) Sample U1438D-19R-CC-11 (~380 mbsf): Plagioclase (?) dissolved and altered to light-red and dark-red-stained Ca-rich zeolites at top, lathwork volcanic lithic fragments with some unaltered plagioclase feldspar, and brown and green rim cements partly filling interparticle pore space (blue). Volcanic fragment on bottom is completely altered to clay minerals. (D) Sample U1438D-29R-5–104 (~475 mbsf): In the center, a chambered foraminifer has been replaced by brown clay and partly filled by dark-red-stained Ca-rich zeolites. The porosity (blue) has likely been exaggerated by swelling clay shrinkage (desiccation) prior to thin-section preparation. This factor and the grain dissolution and pore-filling cements have made recognition of individual grains difficult. (E) Sample 792E-32R-3–81 (~1140 mbsf): The similarity of the alteration and pore-filling mineralogy (brown clay and red Ca-zeolite) in this sample masks original detrital volcaniclastic texture. Porosity (blue) is rare. (F) Sample 792E-54R-3–81 (~1352 mbsf): Pores (blue) in this highly altered volcanic sandstone are mostly secondary, resulting from the dissolution of plagioclase, and other volcanic grains, whereas interparticle porosity has been filled by authigenic Ca-rich zeolites (light-red and red), and clay mineral rims cements. The severe alteration of this sample makes identification of individual sand grain boundaries and types difficult but possible because of the textural differences among grains. (G) Core photo of medium-grained turbidite sequence in U1438E-34R-5 (~1164 mbsf). Note scales in centimeters on left of core image (96–146 cm). Gravity-flow elements marked on images are Bouma (1962) subdivisions Ta, Tb, Tc, Td, and Te (note that there is some complexity from 109 to 113 cm). Note that the sedimentary structure of this bed has been preserved despite alteration.

Integration of Depositional Unit Types and Melt Composition Data

Although vitric components are extremely altered in the matrix of unit III samples, melt inclusions within unaltered phenocrysts were key factors in interpreting the magmatic history of the arc (Fig. 12). Brandl et al. (2017) analyzed plagioclase- and clinopyroxene-hosted melt inclusions from the upper part of unit III (319–495 mbsf) and only clinopyroxene-hosted inclusions from samples below 500 mbsf, where feldspar alteration was more intense. Samples were targeted from intervals with the coarsest and least-altered crystal fractions. A review of the sedimentary facies classes and deposit types for the 47 samples from which melt inclusion data were obtained show the following distribution: disorganized gravel (n = 12); disorganized to graded pebbly sand (n = 28); and disorganized to parallel-stratified sand (n = 7). In terms of bed types, most were taken from gravel-rich debris flows (n = 23) or other gravel-bearing debris flows (n = 14). Fewer were taken from coarse-grained turbidites (n = 4) and classic turbidites (n = 5). When compared to those in debris-flow units, melt inclusions in sandy turbidite facies were more likely to have higher (56–58 wt% SiO_2) or lower (50 wt% SiO_2) average silica contents, or a wider range of values as measured by their standard deviation (i.e., 3.9 and 6.6). These observations indicate that the compositions of sandy units are likely to integrate a wider and more diverse volcanic provenance region than coarser units.

As perhaps expected based on differences in the overall lithology, the thin sections collected to study the petrology of sandy intervals throughout unit III showed a different distribution with respect to bed (depositional unit) types when compared to the melt inclusion sample suite derived from coarser gravel facies. Most of the thin-section samples were taken from partial (n = 57) to full (n = 17) classic (Bouma, 1962) turbidites, and fewer were taken from gravel-rich (>50%) debrites (n = 17) or graded (n = 13) to ungraded (n = 24) gravel-bearing debrites. Fewer still were taken from coarse-grained (Lowe, 1982) turbidites (n = 4) or fine-grained turbidites (n = 7) or graded to ungraded tuff (n = 8). Some (n = 19) were from disrupted/brecciated intervals or intervals that could not be classified.

We looked for trends in the nature of the seven most silicic samples analyzed. Like most of the intervals sampled for petrological studies, they tended to come from the coarser debrite (debris flow with >50% gravel, where maximum grain size is gravel, and bed thickness is >100 cm) and turbidite (coarse-grained sandy turbidite with traction structures, where maximum grain size is gravel, and bed thickness is >100 cm) beds. We prepared thin sections and sampled for zircon analysis (U/Pb age and trace-element geochemistry) from some of these same beds (1438D-22R-6–17cm, 1438D-23R-1–0cm, and 1438E-18R-CC-9cm). Sample 1438D-26R contained no zircons, and 1438E-18R was a zircon-bearing sample. The thin sections generally showed alteration of vitric components, including highly vesicular pumice, with replacement and cementation by clay minerals and zeolites. Minor monocrystalline quartz crystals were also identified in these samples.

ACTUALISTIC MODEL FOR DEEP-MARINE REAR-ARC DEPOSITION AT SITE U1438

Interpretation of Individual Depositional Units

Studies of modern and ancient island-arc volcanoes outline several potential submarine deposit geometries and associated facies: (1) submarine volcanic apron (proximal to distal); (2) submarine fan (proximal to distal); (3) channel fill, potentially associated with 1 and 2; and (4) slump to debris flow, sheets/blankets that taper away from source (e.g., Carey and Sigurdsson, 1984; Busby-Spera, 1985, 1988; Houghton and Landis, 1989; Ballance and Gregory, 1991; Draut and Clift, 2006; Kokelaar and Romagnoli, 1995; Gamberi,

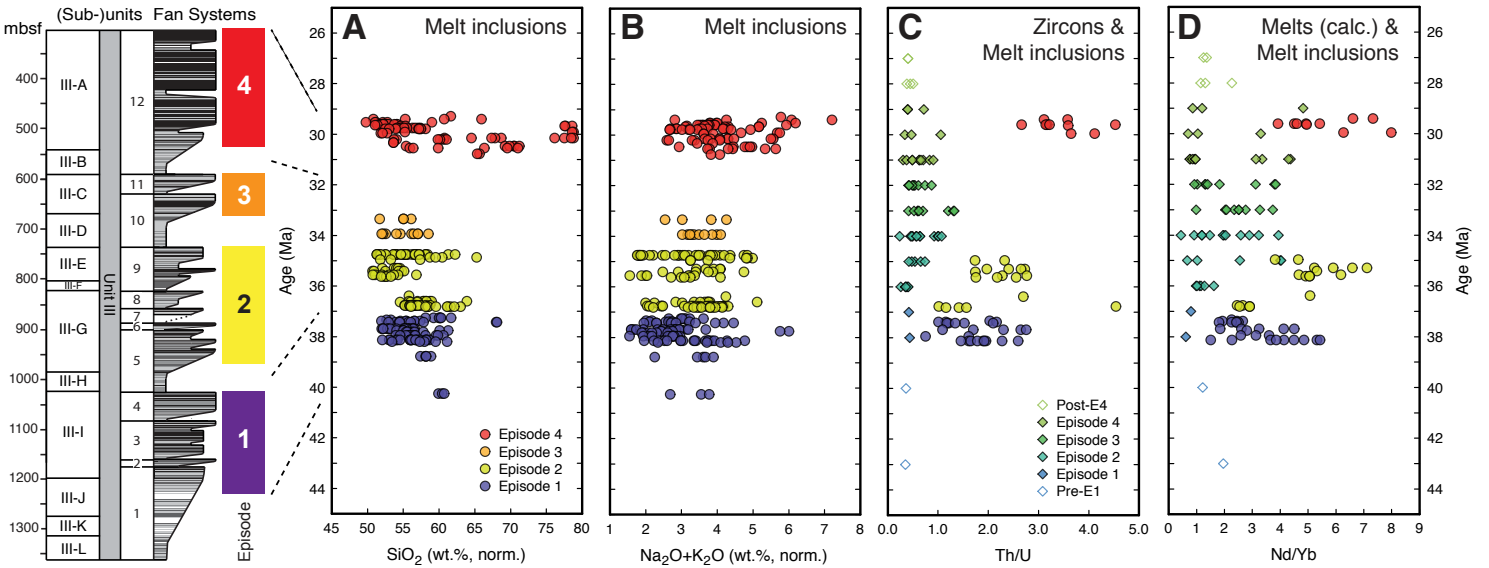

Figure 12. Overview of the depositional episodes of unit III and geochemistry as recorded in major-element (A, B) and trace-element (C, D) compositions of melt inclusions (Brandl et al., 2017) and detrital zircons (Barth et al., 2017). Note the prevalence of (high-Mg) andesitic compositions (>57 wt% SiO_2), low total alkali content ($Na_2O + K_2O$: volatile-free, normalized to 100 wt%), and low (i.e., depleted) trace-element ratios during episode 1 (arc emergence); island-arc tholeiitic compositions during episodes 2 and 3; and silicic (>57 wt% SiO_2), high Th/U, and light rare earth element (LREE)–enriched compositions during episode 4, immediately prior to the onset of arc rifting and backarc spreading. Note that Nd/Yb is used as a tracer for the ratio of light to heavy rare earth elements (LREE/HREE) because La and Pr contents in zircon are very low, and Ce is redox-sensitive. For comparison, Nd/Yb data of melt inclusions and theoretical equilibrium melts calculated from zircon trace-element composition, "Melts (calc.)" (cf. Barth et al., 2017), are shown in D. Symbols in C are the same as in D.

2001; Allen, 2004; Busby, 2004; Busby et al., 2006; Picard et al., 2006; Allen et al., 2007; Chadwick et al., 2008; Gamberi and Marani, 2008; Romagnoli et al., 2009; Casalbore et al., 2010; Watt et al., 2012; Le Friant et al., 2013, 2015; Jutzeler et al., 2017). Furthermore, these geometries and facies are related to the bed-generating mechanisms in arc-proximal to distal deep-marine settings: (1) primary ash falls; (2) volcanic eruption–generated flows/beds; (3) volcano sector collapse–generated flows/beds; (4) seismic shock–generated flows/beds; (5) hurricane/typhoon-generated flows/beds with frequency a function of climate; and (6) debris flows and slumps generated by fault movement and/or seismicity. Thus, the Site U1438 stratigraphy may be a function of sediment supply from subaerial to submarine eruptions (pyroclastics), primary eruption-fed and reworked, as well as erosion of subaerial volcanic edifices (epiclastics), exposed owing to magma supply or tectonics.

Each lamina or thin bed could represent an eruptive event because eruptive products may thin dramatically tens of kilometers away from the arc volcano source into adjacent marine basins. In the Lesser Antilles, for example, individual pyroclastic flows that deposited meter-thick submarine debrite units at the base of a slope on an arc volcano have been linked to turbidity currents that deposited silty graded beds >30 km from their volcanic source (Trofimovs et al., 2008). Other mechanisms are needed to generate the thick gravel-bearing debrite facies documented at Site U1438. Could Site U1438 record event beds related to land-flank slope collapse similar to those documented off Martinique Island on IODP Expedition 340? The results of Expedition 340 and interpretation of these deposits were summarized in Le Friant et al. (2015). With regard to distance from the magmatic arc, Site U1438 is most analogous to Sites U1399 and U1400, which are, respectively, located 78 and 45 km from the source volcano. Site U1399 penetrated a seismically chaotic landslide deposit with cores that exhibit homogenized zones (sandy debrites with sediment intraclasts). Cores did not identify debris avalanche deposits containing blocks from the portion of the subaerial volcano that collapsed into the backarc basin. Such deposits were also not found in more proximal Site U1400, which seismic data indicated should contain records of two events. Sediments at this site exhibited even less deformation and generally fine-grained facies with no apparent distinction between the two events in the core record. Thus, neither site showed evidence for debris avalanche deposits traveling out tens of kilometers into the basin, only evidence for landslide-driven propagation of deformation into the basin; other sites drilled on Expedition 340 in the Lesser Antilles indicated that the debris avalanche deposits are proximal facies and localized at the base of slope of the volcanic edifices. This suggests that zones of deformation may be keys to identifying potential slope-collapse events at Site U1438. Figure F6 in Arculus et al. (2015a) identified intervals of inclined bedding, and we marked those on our Figure 10. We note that the Antilles arc segment is relatively mature (23 m.y. old) in comparison to the stage of development of the arc that supplied unit III debris. Perhaps the Antilles arc segment is best compared to unit II, because the segment exhibits submarine channels to the north of the study area, outside of the zones with submarine debris flows.

Sediment modifications owing to transport (tens of kilometers), as well as postburial lithification and diagenesis limit our ability to link the depositional units that comprise unit III to any of those mechanisms. However, there are some unique compositional traits that we do see that can be linked to eruption mode. For example, petrographic analysis of two unit III samples showed blocky vitric clasts suggesting hydroclastic processes associated with lava-water interaction (e.g., Fisher and Schmincke, 1984). Other intervals with rounded to subrounded volcanic clasts could be linked to volcano emergence and coastal wave processes (e.g., Morrone et al., 2017). Black, opaque-rich tachylitic fragments also indicate subaerial eruptions, whereas orange palagonitized fragments signify reaction with water during or after eruption (e.g., Schiffman et al., 2000). The processes that formed these particles are different from the processes that resulted in their being deposited at the drill site. Some vitric-dominated beds, often highly altered, could be products of pyroclastic fallout. In summary, ours is a very distal, single-hole perspective, where we interpret most of the section to be a product of reworking and mixing.

Insights from Modern Analogues

Draut and Clift (2006) combined data from modern analogues to interpret Jurassic outcrops of intra-oceanic arc facies in Alaska. They focused on the volcanic centers, pointing out the presence of large-scale slumping and mass wasting contributing to the volcanic apron on backscatter sonar images of Mariana volcanoes, as well as evidence for continued downslope reworking in sand waves and channels as elaborated in later works (e.g., Pope et al., 2018; Trofimovs et al., 2008; Watt et al., 2012).

Like Draut and Clift (2006), we looked to modern analogues of the paleo–Kyushu-Palau Ridge arc edifice for guidance in our interpretation of the Site U1438 deposits, but focusing more on the rear-arc perspective. We began with a study by Chadwick et al. (2005), who showed that Anatahan Island, part of the Mariana volcanic arc, sheds volcaniclastic material onto its own volcaniclastic apron. The submarine edifice comprises a 20-km-radius apron around the elongate (10 × 4 km) island, and the apron is also host to numerous smaller vents and extrusions. We note that there is no evidence of magmatic intrusions or eruptive products that would suggest that the coarse unit III volcaniclastics are more proximal volcanic apron deposits, like those of the underlying unit IV (Waldman et al., 2020). In the case of Anatahan, the aprons of adjacent volcanic centers feed into a submarine channel system that apparently transports sediment into the backarc basin (projecting into an area with less bathymetric detail/data). Similar channel systems can be seen to emanate from clusters of arc volcanoes elsewhere along the Mariana arc axis, suggesting that such channel systems may be common submarine elements of intra-oceanic arcs, usually developed in intervolcano topographic lows, and volcano-bounded basins. Thus, a means of funneling coarse sediment from multiple volcanic centers into the backarc region is developed early in arc evolution. There is

also evidence that these submarine channel systems persist during arc rifting and abandonment of remnant arcs (Gardner, 2010).

The vestiges (truncated remnants) of arc volcano flanks and similar submarine canyon/channel systems, some now headless because of rifting of the arc axis, can be seen today along the West Mariana Ridge (Fig. 4B), a remnant arc formed by spreading in the Mariana Trough (Gardner, 2010) and a younger analogue of the Kyushu-Palau Ridge. In each example, the backarc region appears to have been fed sediment by channel systems tapping multiple volcanic centers, some more distal than others. The channels may locally contain gravel (see Supplemental Material, Fig. S4) and ultimately fade into flat plains, likely sediment-covered with local backarc basement. J.V. Gardner (2018, personal commun.) suggested that the resolution of the bathymetric data used in his study might not be high enough to define lobe features at the ends of the channels. Alternatively, there may not be a topographic lobe feature, as found by Carvajal et al. (2017) at the end of a channel on the Navy Fan off Baja California. Their autonomous underwater vehicle collected high-resolution bathymetry that showed the morphology of the channel changes, becoming wider with lower relief without the lobe feature predicted by previous workers. It is noteworthy that cores of sediment in the Navy Channel showed mainly sand, which they interpreted to have been deposited as turbulent flows when well sorted, and as more cohesive gravity flows when the mud content ranged to ~15%.

In the modern Mariana backarc, west of Anatahan Island (Chadwick et al., 2005) and the West Mariana Ridge (Gardner, 2010), the quality of bathymetric data decreases, so we cannot rule out the presence of depositional lobes in these settings. Several studies have amassed statistics on lobe-channel relationships for deep-sea fan systems from around the globe that allow for prediction of lobe size and thickness based on channel width (e.g., Pettinga et al., 2018). The channels extending westward from the West Mariana Ridge and from the Anatahan segment of the Mariana backarc also become wider (as much as 3–5 km wide) as they transition out onto the sedimented plain. Measured relationships plotted in Pettinga et al. (2018) suggest that the Mariana-scale channels could easily produce lobes ranging up to 100 m thick like those we describe at Site U1438 (Fig. 4).

There is limited subsurface information from these modern analogues on the nature of distal deposits ~50 km from the main arc axis, like those recovered at Site U1438 (cf. Kroenke et al., 1980; Hussong et al., 1981). Seismic data show sediment wedges that taper away from the magmatic arc, as shown for Site U1438, but elsewhere that has been limited recovery of drilling-disturbed coarser facies near the volcanic edifice. Laminated to graded, silty to sandy tuffaceous turbidites were recovered at the more distal DSDP Site 456 (Hussong et al., 1981), but no equivalents to the coarse-grained, gravel-rich debrites at Site U1438 were found. The latter could be linked to slope failures and debris avalanches on island-arc volcanoes (e.g., Coombs et al., 2007). These are thought to be products of catastrophic edifice (sector) and slope-apron collapse resulting from rapid volcano growth, producing interlayered weak rocks and destabilizing volcanic (magmatic, seismic) activity. Debris avalanche deposits were recently targeted by IODP Expedition 340 in the Lesser Antilles backarc region, and these cores yielded volcanogenic turbidites and a diverse array of sedimentary units, including debrites, but with variable recovery (Le Friant et al., 2013, 2015; Brunet et al., 2017). These results emphasize the importance of the Site U1438 section, where postdepositional diagenesis and cementation of Eocene to Oligocene volcaniclastic deposits have preserved the clastic textures despite extensive glass and mineral alteration and resulted in enhanced core recovery rate owing to the high degree of induration.

Higher in the section at Site U1438, there are other links to the work of Gardner (2010), who documented evidence for nonchannelized sediment transport in the form of downslope creep. He identified and mapped expansive wrinkled surfaces, creep-lobes, on the flank of the Mariana Ridge within the channel-bearing region (Fig. 4B). Gardner (2010) cited limited seismic evidence as indicating that these slightly deformed lobes can reach thicknesses of up to 300 m. A candidate for the distal equivalent of such a deformed lobe exists in the core recovered at Site U1438, where a zone of compressional deformation (largely reverse faulting) starts at 200 mbsf and extends down to ~300 mbsf within unit II. The deformed interval is also a zone of poor core recovery encountered in Holes B and Hole D (see fig. F19 *in* Arculus et al., 2015a). The gravel-rich facies below the deformed zone suggest that a lobe might have partly filled a channel. This deformed interval in the basal part of unit II is considered to have been deposited in the synrift stage, similar to the time frame and setting in which the relict bathymetric features described by Gardner (2010) were created during arc rifting and formation of the Mariana Trough and remnant West Mariana Ridge. The arc volcaniclastic sequence in the Amami Sankaku Basin, however, is covered by >180 m of (postrifting) hemipelagic sediments that may make it difficult or impossible to discern relict channel features like those seen in the younger Mariana system (Gardner, 2010; Chadwick et al., 2005).

Our analysis indicates that volcaniclastic debris was shed from the Kyushu-Palau Ridge (the initial Izu-Bonin-Mariana arc) in submarine sediment gravity flows perhaps triggered by high-volume volcanic eruptions, tectonic/seismic activity, or sector collapses like those documented in the active Kermadec arc (Chadwick et al., 2008). These gravity flows were transported via channels to form submarine lobes in the rear-arc basin.

DEPOSITIONAL MODEL—CHANNEL-FED LOBE SYSTEMS

The simplified depositional model proposed for unit III shown in Figure 4A is based on bathymetric imagery of active volcanoes and deactivated segments of the Mariana arc system, west of the West Mariana Ridge described above (Fig. 1). Applying the clastic facies criteria of Mutti and Normark (1987), the 12 subunits in unit III at Site U1438 exhibit characteristics of prograding submarine lobes fed by submarine channels (Fig. 3). Seismic data in the area are limited, but their pattern is consistent with lobe-channel interpretation. The seismic lines crossing Site U4138 (Figs. S2 and S3 [footnote 1]) show that, although the reflectors in the upper parts of unit III are horizontal, they

are not continuous for more than ~10 km. This fits with our potential depositional analogue pictured in Figure 4B, where channels emanating from the volcanoes that make up the West Mariana Ridge coalesce to create channels with a maximum width of 10 km at a distance of 50 km from the ridge axis (upper arrow in Fig. 4). It would then be expected that during accumulation of unit III, such feeder channels would have meandered back and forth across the downslope regions over time, limiting the horizontal extent of coherent layering (channel facies reflectors) to no more than 10 km, as observed in the seismic data. Lobe (subunit) thickness variations within the cored section (see below) are consistent with lobe lateral migration and overlap, building a thick complex of lobes or fan succession (unit III), similar to what is depicted in Covault (2011) after Mutti and Ricci Lucchi (1972).

The overlapping of lobes in the model (Fig. 4A) may be a result of distributary channel switching within the lobe system that resulted in finer and more distal lobe facies being deposited for short periods of time. Alternatively, the pattern could be explained by pulsed sediment input into the basin as indicated by the alternate lobe geometry in Figure 4A as discussed below. These lobes may be linked to autocyclic switching or periods of edifice buildup and subsequent collapse and slope degradation, but we cannot rule out the influence of other climatic (eustasy, typhoon frequency?) and tectonic (uplift, seismicity?) processes that would affect sediment supply.

Autocyclic switching would result in alternating lobe-axis (coarser) and lobe-margin (finer) sedimentation. In the case of vertical aggradation of material, the coarse-fine alternation in the unit III stratigraphic column would be a function of allocyclic changes (pulses) in supply of coarse sediment not associated with channel avulsion (e.g., Jobe et al., 2020). The allocyclic pulses might result from the tempo of magmatic processes in the case of this magmatic arc example. Modeling studies (Burgess et al., 2019) indicate that differentiating between autocyclic and allocyclic controls on submarine fan successions is difficult with limited outcrop data, which in the case of Site U1438 is a single vertical stratigraphic column (slightly offset series of cored holes; Fig. 3).

Applying this model to unit III, it broadly consists four packages (labeled episodes 1–4 in Fig. 10) of stacked lobe systems (comprising a lobe complex), and coarse sediment accumulation can be identified within unit III, separated by thick intervals of thin, fine-grained turbidites (Fig. 3). An episode could be equivalent to an eruptive period, a term proposed by Fisher and Schmincke (1984) to describe broader-scale magmatism lasting up to millions of years (allocyclicity). Each of the episodes has a different character, likely reflecting a combination of autocyclic or allocyclic controls associated with volcano and channel development and evolution, such as spatial migration of volcanic centers and distributary channel switching.

Episode 1 represents the initial construction of the Kyushu-Palau Ridge arc edifices to the east and progressive increase in supply of coarse material to Site U1438 (Fig. 2). Episode 2 has the lowest debrite content, with most lobes terminating in a channel-lobe transitional facies without a capping channel-facies deposit. Episodes 1, 2, and 4 comprise composite sequences of prograding lobe facies without distal lobe facies.

The age-depth model created from shipboard micropaleontology and paleomagnetic datums and reinforced by U-Pb zircon geochronology suggests that deposition of sediment packages was indeed episodic (Fig. 10). Episodes 1 and 2 were each deposited over periods of ~2 m.y., whereas episodes 3 and 4 were deposited over periods of ~1.6 m.y. Intervening finer-grained units range from 300 k.y. between episodes 1 and 2 to ~1 m.y. between episodes 2 and 3 and between episodes 3 and 4. This 1–2 m.y. periodicity is an order of magnitude greater than the 100–300 k.y. estimated from tephra records of the Kamchatka-Kuril and Aleutian subaerial arcs (Prueher and Rea, 2001), but it is consistent with ages of arc volcanoes (e.g., Harford et al., 2002; Watts et al., 2012; Wilson et al., 1995). The reason for this life span is uncertain but may record the time frame over which a single magmatic feeder system remains stable in an otherwise active geodynamic setting. The increasing proportion of coarse material toward the top of the section is consistent with a larger or more proximal volcanic source during episode 4. This fits with the observation by Bloomer et al. (1989), who noted that the spacing (50–70 km) and degree of emergence of arc volcanoes increase through time as the arc matures, but this pattern is by no means universal. A second explanation would be that the uppermost unit was fed by rear-arc volcanoes, which are often associated with initial arc rifting prior to backarc spreading (Fig. 2). The phase preceding backarc opening could be characterized by inflow of hot and fertile mantle into the wedge and increased magmatic productivity, as indicated by high depositional rates in conjunction with geochemical changes in zircon and melt compositions (Barth et al., 2017; Brandl et al., 2017; Hamada et al., 2020).

Overall, we consider the succession to record the evolution of the arc superimposed on a stepwise record of 3–4 individual episodes (1, 2+3?, 4). Periodicity within the succession ranges from an eruptive scale of 100–1000 yr, including eruption-related and non-eruption-related sector collapse, to a longer scale up to millions of years, probably related to life of individual edifices and switching of source volcanoes feeding into channel systems.

DEPOSITIONAL CYCLES AND OCEANIC ARC MAGMATIC EVOLUTION

Ishizuka et al. (2011) demonstrated from dredge and shallow drill core samples that the latest stage of volcanism in the Kyushu-Palau Ridge remnant arc was characterized by lavas more enriched in alkali and light rare earth elements (LREEs) than the Izu-Bonin arc front. They also showed that Kyushu-Palau Ridge bathymetry preserves rear-arc chains, similar to the mode of occurrence of relatively enriched lavas in the modern morphologically and geochemically asymmetric arc. Ishizuka et al. (2011) concluded that the Kyushu-Palau Ridge became asymmetrical and developed distinctive, enriched rear-arc volcanoes at some point after ca. 35 Ma.

Site U1438 unit III melt inclusion and zircon data sets (Barth et al., 2017; Brandl et al., 2017; Hamada et al., 2020) are linked to the four depositional episodes defined here (Figs. 12 and 13), recording the relationship of these

depositional episodes to the evolution of petrologic asymmetry in the arc. Detrital zircons range in measured age from 43 to 27 Ma but were recovered predominantly from the upper part of unit III (<800 mbsf), and these detrital zircons have crystallization ages younger than 35 Ma. Most intervals have a range of zircon ages ~2–4 m.y. in excess of the calculated maximum depositional age of the host interval; this observation indicates that at least the younger parts of unit III (episodes 3 and 4) are products of substantial stratigraphic mixing, containing both primary and reworked volcanic materials. This mixing recorded by U/Pb ages is of the same order as the time interval of each depositional episode, placing limits on the precision of correlation between episodes and construction of any single volcanic edifice. Nevertheless, trends in melt inclusion and zircon compositional data allow us to infer in a general way the link between sedimentation and arc evolution along the Kyushu-Palau Ridge.

Episodes 1 (bottom) and 4 (top) are clearly geochemically distinct, with the first reflecting high-Mg andesitic volcanism following arc inception and the latter being silicic, probably reflecting progressive crustal thickening and development of silicic and enriched rear-arc volcanism (Figs. 12 and 13). Episodes 2 and 3 are somewhat intermediate, but it is hard to say if they are distinct from the other episodes with statistical significance (cf. Hamada et al., 2020). Episode 4 corresponds to the initial phase of arc rifting that resulted in

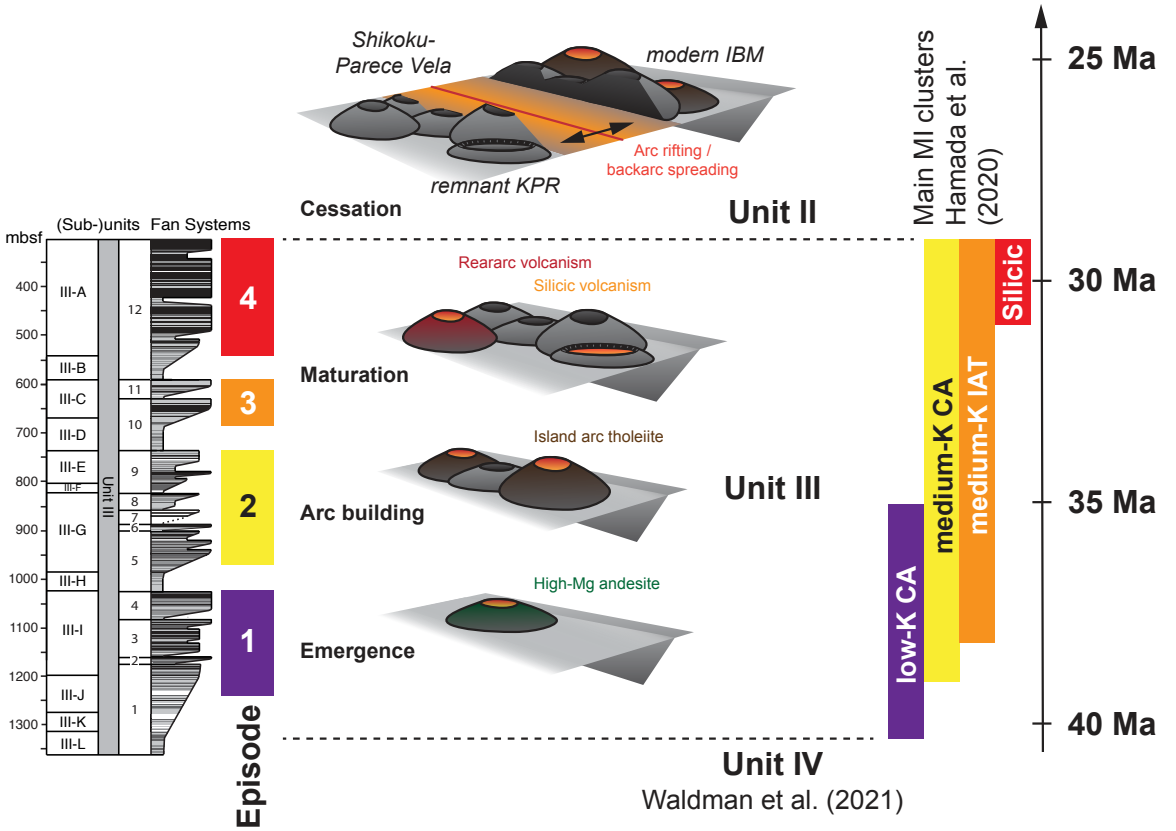

Figure 13. Overview of the depositional episodes of unit III compared to Kyushu-Palau Ridge remnant arc evolution, melt evolution (as illustrated by the main melt inclusion [MI] clusters as defined by Hamada et al., 2020), and age. Data show changes in melt composition associated with each episode as defined in this study: Episode 1 reflects the arc emergence with low-K calc-alkaline (CA) melts at ca. 40 Ma and arc maturation (medium-K calc-alkaline and island-arc tholeiitic [IAT] melts) during episodes 2 and 3. Episode 4 samples include silicic melts that were erupted immediately prior and during arc rifting at ca. 30 Ma. IBM—Izu-Bonin-Mariana arc; KPR—Kyushu-Palau Ridge arc; mbsf—meters below seafloor.

high clastic sediment supply, and pumice and dacitic-rhyolitic melt inclusions (Figs. 12 and 13).

The evolving petrologic character of the volcanic arc is clearly recorded in episodes 3 and 4 (Figs. 12 and 13), as indicated by: (1) the more common occurrence of dacite and rhyolite melt inclusions shown by Brandl et al. (2017) to have LREE-enriched compositions after 37 Ma, (2) the more common occurrence of detrital zircons, and (3) the relatively enriched, high Th/U, and LREE-enriched melts (as reflected in Nd/Yb) inferred from zircon compositions (Figs. 12C and 12D). Melt inclusions from upper unit III collected from samples with depositional ages younger than 37 Ma comprise a medium potassic, LREE-enriched suite similar to Kyushu-Palau Ridge dredge samples and the modern rear arc (Brandl et al., 2017). Dacitic to rhyolitic melt inclusions recovered from the uppermost part of unit III record more fractionated melt compositions in the arc (Fig. 12A). The common occurrence of detrital zircons in volcanic sandstones over the same time interval (<35 Ma; Barth et al., 2017) also indicates that relatively cool and silicic melts were being produced in the arc; the zircon enrichment in Nd/Yb and Th/U implies growth from silicic melts with Nd/Yb >1, that is, zircon-saturated silicic melts with rear-arc compositional affinity.

The occurrence of such dacitic to rhyolitic melts, recorded in melt inclusions and inferred from zircon compositions, may also be linked to the occurrence of gravel in the cores. The co-occurrence of fractionated melts and coarser debrites implies that some silicic eruptions were explosive. Volcanism during episodes 3 and 4 (<35 Ma) is characterized by the disappearance of low-K calc-alkaline melt compositions and the appearance of high-K and/or silicic melts, especially during episode 4 (cf. Hamada et al., 2020). More silicic magmatism in episode 4 corresponds to more explosive magmatism and the development of calderas, and/or the development of arc asymmetry and rear-arc chains.

In summary, the lobe system of episode 1 represents the sedimentary record of initial arc edifice building (Fig. 2) and is associated in time with a geochemical shift from dominantly high-Mg and calc-alkaline volcanism to coeval tholeiitic and calc-alkaline arc volcanism around 37 Ma (cf. Brandl et al., 2017; Hamada et al., 2020). This age is consistent with the age of the end of the relatively magnesian (more magnesian relative to younger Izu-Bonin arc front) basalt to andesitic magmatism on the Bonin Ridge, which had been active between 45 and 37 Ma (Ishizuka et al., 2020). The change from episode 2 to 3, ca. 35 Ma (Fig. 2), is associated with an increase in quartz and zircon recovered in mineral separates (Brandl et al., 2017; Barth et al., 2017), and so we infer the onset of relatively abundant silicic volcanism at or immediately after ca. 35 Ma. This link between coarsening sediment episodes and onset of abundant silicic volcanism is consistent with the model of Ishizuka et al. (2011), wherein rear-arc volcanism in the Kyushu-Palau Ridge after ca. 35 Ma was more strongly influenced by high-Th and LREE-enriched (deep subduction) components (Fig. 2). More vigorous rear-arc volcanism after 35 Ma likely brought sediment sources closer to the drill site and provided a silicic source for the high-Th and LREE-enriched silicic melts inferred from the zircon data (Barth et al., 2017) and the dacitic to rhyolitic melt inclusions reported by Brandl et al. (2017) after 31 Ma.

The rear-arc compositional signals in our data are not surprising, given the parallels with modern Izu-Bonin-Mariana uplift and incipient rifting and the situation we envision for episodes 3 into 4 (Fig. 2). The modern Izu-Bonin-Mariana arc is magmatically asymmetric, with a low-K and LREE-depleted volcanic front, and relatively enriched medium-K series in the rear-arc volcanic chains, where arc volcanism creates melts with higher alkali content, especially K (Nichols et al., 2012). Upper unit III melt inclusions and model melts from zircon compositions both suggest rear-arc sources (Figs. 12 and 13). The seafloor morphology of the Kyushu-Palau Ridge east of Site U1438 (Fig. 1) also suggests the development of rear-arc chains.

Also, in our data set, we see a trend toward higher alkali ($Na_2O + K_2O$) contents with younger age (Fig. 12). Hamada et al. (2020) showed a disappearance of low-K melts past 35 Ma, appearance of medium-K melts at 39–38 Ma, and overall geochemical evolution of melts with time from 40 Ma to 30 Ma indicated by increases in SiO_2 and K_2O and decreases in MgO. Furthermore, Th/U and Th/Nb (not shown) increase with decreasing age, indicating a higher impact of fluids and/or melts derived from sediments, which is typical for greater slab depth and thus increasing distance from the trench, as expected with rear-arc magmatic sources (cf. Brandl et al., 2017). Decreasing Ba/Th also suggests rear-arc sources in that Ba is used as a tracer for fluids derived from shallow subduction.

CORRELATION WITH IZU-BONIN-MARIANA FOREARC AND REAR-ARC DEPOSITIONAL RECORDS

Rifting and seafloor spreading in the Shikoku and Parece Vela backarc basins separated the Kyushu-Palau Ridge, an inactive remnant arc, from the active Izu-Bonin arc (Ishizuka et al., 2011). Seafloor spreading in the Shikoku Basin was oblique, so a prerift palinspastic restoration of the magmatic arc segment that sourced the Site U1438 Eocene to Oligocene succession would place that segment near sites drilled during ODP Leg 126 in the Izu-Bonin forearc (e.g., Deschamps and Lallemand, 2002). The stratigraphic records at these forearc sites (787, 792, 793) show high rates of volcanic sediment accumulation during rifting and initial seafloor spreading from 29 to 27 Ma (Taylor et al., 1990), in a time frame that corresponds to unit II at Site U1438. Only Site 793 penetrated a 31–29 Ma stratigraphic record (equivalent to episode 4 at Site U1438) above forearc basement. It consists of ~300 m of very thick (up to 5–10 m), volcanic pebbly sandstone and pebble conglomerate with large floating intraclasts and volcanic cobbles interpreted by shipboard scientists as products of submarine gravity flows; these include debris flows and turbidity currents with rounded arc-derived clasts produced by coastal and nearshore erosion, reworked pyroclasts, and shallow-marine limestone and biogenic debris (red algae, benthic foraminifers) delivered via submarine channels(?) to the forearc, potentially aided by global falling sea level (Taylor et al., 1990).

Subsequent sea-level studies, as summarized in Spasojevic and Gurnis (2012), continued to show a major inflection point around 30 Ma, but there is also the potential for regional tectonic uplift prior to rifting. Sketched examples of these debrite and turbidite beds (Taylor et al., 1990) are similar to those encountered at Site U1438 (Johnson et al., 2017). These deposits should differ from those at Site U1438 by not bearing clasts with geochemical signatures of rear-arc magmatism. We note that the actively rifting and extending Izu-Bonin segment of the Izu-Bonin-Mariana arc shows submarine channels extending in some places from the arc, across the forearc, and into the trench (see area north of Site 793 in Fig. 1). Site 787 was located in one of these erosive channels to expedite penetration of older forearc sedimentary sections.

Other recent forearc drilling on IODP Expedition 352, ~500 km to the south of Site 793, recovered thin (few tens of meters or less) time-equivalent sections to the 33–29 Ma section at Site U1438. The range of lithologies at Sites U1439, U1440, and U1442 includes chalk, tuff, volcanic sandstone, and conglomerate (Robertson et al., 2018). Their connection to Site U1438 is more speculative than Site 793 because of the added distance.

Site U1438 is not unique in recording the rear-arc record of magmatic arc initiation and development. ODP Site 1201 is located in a similar rear-arc position as Site U1438 further south along the Kyushu-Palau Ridge (Salisbury et al., 2002). We note that the stratigraphy at this site parallels that of Site U1438: Facies in cores 1201D-43R to 1201D-45R are similar to those described by Waldman et al. (2021) in unit IV at Site U1438, transitioning up into 400+ m of Eocene to Oligocene gravity-flow deposits (cores 1201D-42R to 1201D-1R) similar to those of unit III at Site U1438. Detailed comparison of the stratigraphic sections at Sites U1438 and 1201 is hampered by a lack of detailed sedimentary facies analysis similar to that conducted by Johnson et al. (2017), limited success with zircon geochronology and chemistry (limited to one sample $^{206}Pb^*/^{238}U$ age of 35.0 ± 1.1 Ma; Barth et al., 2017), and geochemical analyses focused mostly on the basement rocks at this site, with a few discrete clast analyses (bulk and trace element) from the unit III–equivalent gravity-flow deposits (Savov et al., 2006).

There is ample room for continued work on these sections. For example, we provide a framework in which to evaluate future studies of the bulk geochemistry of volcaniclastic sandstones in the Site U1438 succession (Laxton, 2016) and their comparison to time-equivalent forearc (Gill et al., 1994; Robertson et al., 2018) and backarc (Salisbury et al., 2002; Savov et al., 2006) data sets, as well as more detailed comparative facies analysis of Site 1201 and 793 cores with Site U1438 time equivalents.

IMPLICATIONS FOR INTERPRETATION OF OTHER ANCIENT INTRA-OCEANIC SUCCESSIONS

The discrimination of intra-oceanic backarc versus forearc basin successions in the rock record is usually demonstrated through the geochemistry of the igneous basement rocks, e.g., backarc basin or forearc basin basalt, upon which the arc-generated deposits accumulated (e.g., Critelli et al., 2002). With increasing proximity to the arc-axis volcanos, there are intrusive or effusive volcanic rocks associated with volcanic apron facies (e.g., Allen et al., 2007). As outlined in Marsaglia (1995), young, unconsolidated facies equivalents of Site U1438 deposits thwarted core recovery during previous DSDP and ODP rotary drilling. Diagenetic modification was key to enhanced lithification and core recovery at Site U1438 (Johnson et al., 2017; Waldman et al., 2021).

Interpretations of intra-oceanic arc-related successions accreted to continental margins or caught up in collisional orogens are often contentious (e.g., Pavlis et al., 2019; Draut and Clift, 2013). Geodynamic models suggest that one also needs to take into account the nuances of subduction/accretion and likelihood of preservation of forearc/arc/backarc successions in collision zones, with a higher probability of thicker arc-axis zones being scraped off and thinner ocean basins being subducted (e.g., Boutelier et al., 2003). The data that we present here might prove useful in interpreting sedimentary successions deposited ~50 km distant from the magmatic arc, where outcrops (or core) permit facies analysis, and delineation of episodes (lobe complexes) and componentry allows for advanced glass and mineral geochemical analyses. We know that similar facies were recovered ~700 km to the south of our study area at Site 1201. Other potential successions that might lend themselves to interpretation include Cretaceous terranes incorporated into the Himalayan orogen (Robertson and Collins, 2002; Robertson and Degnan, 1994) and Jurassic to Cretaceous oceanic-arc terranes on Baja California (Busby-Spera, 1988; Busby et al., 2006; Critelli et al., 2002).

CONCLUSIONS

The excellent percentage and quality of core recovered at IODP Site U1438 allowed for our detailed sedimentological and combined geochemical study of intra-oceanic arc evolution from the early stages of development ca. 40 Ma until arc rifting ca. 29 Ma. Previously defined subunits were grouped here into four thicker packages (episodes) of coarse sediment gravity flows (debrites to turbidites), each deposited over time frames of ~1.6–2 m.y. and separated by ~1 m.y. intervals of thin-bedded, fine-grained turbidites. An interpretive organization of the unit III stratigraphic section was made using lobe models developed for submarine fans and observations of bathymetry and implied submarine sediment routing around modern arc volcanoes and backarc regions.

Postburial diagenesis progressively modified volcanic components within the succession, contributing to lithification, which in turn promoted higher core recovery and preservation of sedimentary textures and structures. Luckily, the alteration was not complete, especially in the coarser sediments, preserving some mineralogy and melt inclusions that could be used for geochemical and isotopic analyses that we then related to the depositional episodes. Sediments in episode 1 at the base of unit III form a coarsening-upward record of initial arc development and high-Mg andesite volcanism with a magmatic change

at around 37 Ma to dominantly island-arc tholeiitic volcanism that continued into episode 2. The onset of relatively abundant silicic volcanism at ca. 35 Ma corresponds with the change from episode 2 to 3. Enhanced rear-arc volcanism during episode 4 produced coarser volcanic debris channel facies and silicic volcanism ranging in composition from andesitic to rhyolitic with enhanced zircon content. The coarse conglomerate and debrite facies of episode 4 are similar to those encountered in the Izu-Bonin forearc, suggesting that there was widespread uplift and erosion of the arc as extension and silicic magmatism commenced, analogous to the current phase of Izu-Bonin arc extension and rifting (e.g., Sumisu Rift).

This study covered over 10 m.y. of intra-oceanic arc history, building up from grain and bed scales. Although based on a single drill site perspective, the transported nature of the sedimentary succession yielded depositional and magmatic insights on a regional scale that can be tested by future IODP drilling and applied to ancient intra-oceanic successions accreted and incorporated into continental orogens.

ACKNOWLEDGMENTS

Detailed comments by Peter Clift and Alastair Robertson were greatly appreciated and improved the manuscript. This work was supported by awards from Ocean Leadership and the National Science Foundation to K.M. Marsaglia (OCE-1503694) and from the Geological Society of America to K. Johnson. Barth acknowledges NSF grant OCE-1558830. Thanks also go to Sharon Allen and David Buchs for their thoughtful reviews of an earlier version of this manuscript, to Bill Gardner for his contributions to analogue development, and to Jamstec for access to the legacy seismic data. This research used samples and data provided by the International Ocean Discovery Program (IODP).

REFERENCES CITED

Allen, S.R., 2004, The Parnell Grit beds revisited: Are they all the products of sector collapse of western subaerial volcanoes of the Northland volcanic arc?: New Zealand Journal of Geology and Geophysics, v. 47, p. 509–524, https://doi.org/10.1080/00288306.2004.9515073.

Allen, S.R., Hayward, B.W., and Matthews, E., 2007, A facies model for a submarine volcaniclastic apron: The Miocene Manukau Subgroup, New Zealand: Geological Society of America Bulletin, v. 119, p. 725–742, https://doi.org/10.1130/B26066.1.

Arculus, R., Ishizuka, O., Bogus, K., and the Expedition 351 Scientists, 2015a, Proceedings International Ocean Discovery Program (IODP), Volume 351: Izu-Bonin-Mariana Arc Origins: College Station, Texas, International Ocean Discovery Program, https://doi.org/10.14379/iodp.proc.351.201.2017.

Arculus, R.J., Ishizuka, O., Bogus, K.A., Gurnis, M., Hickey-Vargas, R., Aljahdali, M.H., Bandini-Maeder, A.N., Barth, A.P., Brandl, P.A., Drab, L., do Monte Guerra, R., Hamada, M., Jiang, F., Kanayama, K., Kender, S., Kusano, Y., Li, H., Loudin, L.C., Maffione, M., Marsaglia, K.M., McCarthy, A., Meffre, S., Morris, A., Neuhaus, M., Savov, I.P., Sena, C., Tepley, F.J., van der Land, C., Yogodzinski, G.M., and Zhang, Z., 2015b, A record of spontaneous subduction initiation in the Izu-Bonin-Mariana arc: Nature Geoscience, v. 8, p. 728–733, https://doi.org/10.1038/ngeo2515.

Ballance, P.F., and Gregory, M.R., 1991, Parnell Grits—Large subaqueous volcaniclastic gravity flows with multiple particle support mechanisms, *in* Fisher, R.V., and Smith, G.A., eds., Sedimentation in Volcanic Settings: Society for Sedimentary Geology (SEPM) Special Publication 45, p. 189–200, https://doi.org/10.2110/pec.91.45.0189.

Barth, A.P., Tani, K., Meffre, S., Wooden, J.L., Coble, M.A., Arculus, R.J., Ishizuka, O., and Shukle, J.T., 2017, Generation of silicic melts in the early Izu-Bonin arc recorded by detrital zircons in proximal arc volcaniclastic rocks from the Philippine Sea: Geochemistry Geophysics Geosystems, v. 18, p. 3576–3591, https://doi.org/10.1002/2017GC006948.

Bloomer, S.H., Stern, R.J., and Smoot, N.C., 1989, Physical volcanology of the submarine Mariana and Volcano arcs: Bulletin of Volcanology, v. 51, p. 210–224, https://doi.org/10.1007/BF01067957.

Bouma, A.H., 1962, Sedimentology of Some Flysch Deposits: A Graphic Approach to Facies Interpretation: Amsterdam, Netherlands, Elsevier Publishing Company, 168 p.

Boutelier, D., Chemenda, A., and Burg, J.-P., 2003, Subduction versus accretion of intra-oceanic volcanic arcs: Insight from thermo-mechanical analogue experiments: Earth and Planetary Science Letters, v. 212, p. 31–45, https://doi.org/10.1016/S0012-821X(03)00239-5.

Brandl, P.A., Hamada, M., Arculus, R.J., Johnson, K., Marsaglia, K.M., Ishizuka, O., and Savov, I., 2017, The arc arises: The links between volcanic output, arc evolution, and melt composition: Earth and Planetary Science Letters, v. 461, p. 73–84, https://doi.org/10.1016/j.epsl.2016.12.027.

Brunet, M., Moretti, L., Anne Le Friant, A., Mangeney, A., Domingo, E., Nieto, F., and Bouchut, F., 2017, Numerical simulation of the 30–45 ka debris avalanche flow of Montagne Pele'e volcano, Martinique: From volcano flank collapse to submarine emplacement: Natural Hazards, v. 87, p. 1189–1222, https://doi.org/10.1007/s11069-017-2815-5.

Burgess, P.M., Masiero, I., Toby, S.C., and Duller, R.A., 2019, A big fan of signals? Exploring autogenic and allogenic process and product in a numerical stratigraphic forward model of submarine-fan development: Journal of Sedimentary Research, v. 89, p. 1–12, https://doi.org/10.2110/jsr.2019.3.

Busby, C.J., 2004, Continental growth at convergent margins facing large ocean basins: A case study from Mesozoic convergent-margin basins of Baja California, Mexico: Tectonophysics, v. 392, p. 241–277, https://doi.org/10.1016/j.tecto.2004.04.017.

Busby, C.J., Fackler-Adams, B.N., Matinson, J., and Deoreo, S., 2006, View of an intact oceanic arc, from surficial to mesozonal levels: Cretaceous Alisitos arc, Baja California: Journal of Volcanology and Geothermal Research, v. 149, p. 1–46, https://doi.org/10.1016/j.jvolgeores.2005.06.009.

Busby-Spera, C.J., 1985, A sand-rich submarine fan in the Lower Mesozoic Mineral King caldera complex, Sierra Nevada, California: Journal of Sedimentary Petrology, v. 55, p. 376–391, https://doi.org/10.1306/212F86D9-2B24-11D7-8648000102C1865D.

Busby-Spera, C.J., 1988, Evolution of a Middle Jurassic back-arc basin, Cedros Island, Baja California: Evidence from a marine volcaniclastic apron: Geological Society of America Bulletin, v. 100, p. 218–233, https://doi.org/10.1130/0016-7606(1988)100<0218:EOAMJB>2.3.CO;2.

Carey, S., and Sigurdsson, H., 1984, A model of volcanogenic sedimentation in marginal basins, *in* Kokelaar, B.P., and Howells, M.F., eds., Marginal Basin Geology: Volcanic and Associated Sedimentary and Tectonic Processes in Modern and Ancient Marginal Basins: Geological Society [London] Special Publication 16, p. 37–58, https://doi.org/10.1144/GSL.SP.1984.016.01.04.

Carey, S., Tony Maria, T., and Cornell, W., 1998, Processes of volcaniclastic sedimentation during the early growth stages of Gran Canaria based on sediments from Site 953, *in* Weaver, P.P.E., Schmincke, H.-U., Firth, J.V., and Duffield, W., eds., Proceedings of the Ocean Drilling Program, Scientific Results, Volume 157: College Station, Texas, Ocean Drilling Program, p. 183–200.

Carvajal, C., Paull, C.K., Caress, D., Fildani, A., Lundsten, E., Anderson, K., Maier, K.L., McGann, M., Gwiazda, R., and Herguera, J.C., 2017, Unraveling the channel-lobe transition zone with high-resolution AUV bathymetry: Navy Fan, offshore Baja California, Mexico: Journal of Sedimentary Research, v. 87, p. 1049–1059, https://doi.org/10.2110/jsr.2017.58.

Casalbore, D., Romagnoli, C., Chiocci, F., and Frezza, V., 2010, Morpho-sedimentary characteristics of the volcaniclastic apron around Stromboli volcano (Italy): Marine Geology, v. 269, p. 132–148, https://doi.org/10.1016/j.margeo.2010.01.004.

Chadwick, W.W., Embley, R.W., Johnson, P.D., Merle, S.G., Ristau, S., and Bobbitt, A., 2005, The submarine flanks of the Anatahan Volcano, commonwealth of the Northern Mariana Islands: Journal of Volcanology, v. 146, p. 8–25, https://doi.org/10.1016/j.jvolgeores.2004.11.032.

Chadwick, W.W., Jr., Wright, I.C., Schwarz-Schampera, U., Hyvernaud, O., Reymond, D., and de Ronde, C.E.J., 2008, Cyclic eruptions and sector collapses at Monowai submarine volcano, Kermadec arc: 1998–2007, Geochemistry, Geophysics, Geosystems, v. 9, Q10014, https://doi.org/10.1029/2008GC002113.

Clift, P.D., and Lee, J., 1998, Temporal evolution of the Mariana arc during rifting of the Mariana Trough traced through the volcaniclastic record: The Island Arc, v. 7, p. 496–512, https://doi.org/10.1111/j.1440-1738.1998.00206.x.

Clift, P.D., Degnan, P.J., Hannigan, R., and Blusztajn, J., 2000, Sedimentary and geochemical evolution of the Dras forearc basin, Indus suture, Ladakh Himalaya, India: Geological Society of America Bulletin, v. 112, p. 450–466, https://doi.org/10.1130/0016-7606(2000)112<450:SAGEOT>2.0.CO;2.

Clift, P.D., Draut, A.E., Kelemen, P.B., Blusztain, J., and Greene, A., 2005, Stratigraphic and geochemical evolution of an oceanic arc upper crustal section: The Jurassic Talkeetna Volcanic

Formation, south-central Alaska: Geological Society of America Bulletin, v. 117, p. 902–925, https://doi.org/10.1130/B25638.1.
Coombs, M.L., White, S.M., and Scholl, D.W., 2007, Massive edifice failure at Aleutian arc volcanoes: Earth and Planetary Science Letters, v. 256, p. 403–418, https://doi.org/10.1016/j.epsl.2007.01.030.
Covault, J.A., 2011, Submarine fans and canyon-channel systems: A review of processes, products, and models: Nature Education Knowledge, v. 3, no. 10, p. 4.
Critelli, S., Marsaglia, K.M., and Busby, C.J., 2002, Tectonic history of a Jurassic backarc-basin sequence (the Gran Cañon Formation, Cedros Island, Mexico), based on compositional modes of tuffaceous deposits: Geological Society of America Bulletin, v. 114, p. 515–527, https://doi.org/10.1130/0016-7606(2002)114<0515:THOAJB>2.0.CO;2.
Deschamps, A., and Lallemand, S., 2002, The West Philippine Basin: An Eocene to early Oligocene back arc basin opened between two opposed subduction zones: Journal of Geophysical Research, v. 107, no. B12, 2322, https://doi.org/10.1029/2001JB001706.
Draut, A.E., and Clift, P.D., 2006, Sedimentary processes in modern and ancient oceanic arc settings: Evidence from the Jurassic Talkeetna Formation of Alaska and the Mariana and Tonga arcs, western Pacific: Journal of Sedimentary Research, v. 76, p. 493–514, https://doi.org/10.2110/jsr.2006.044.
Draut, A.E., and Clift, P.D., 2013, Differential preservation in the geologic record of intraoceanic arc sedimentary and tectonic processes: Earth-Science Reviews, v. 116, p. 57–84, https://doi.org/10.1016/j.earscirev.2012.11.003.
Fisher, R.V., and Schmincke, H.-U., 1984, Pyroclastic Rocks: Berlin, Springer-Verlag, 472 p., https://doi.org/10.1007/978-3-642-74864-6.
Gamberi, F., 2001, Volcanic facies associations in a modern volcaniclastic apron (Lipari and Vulcano offshore, Aeolian island arc): Bulletin of Volcanology, v. 63, p. 264–273, https://doi.org/10.1007/s004450100143.
Gamberi, F., and Marani, M., 2008, Controls on Holocene deep-water sedimentation in the northern Gioia Basin, Tyrrhenian Sea: Sedimentology, v. 55, p. 1889–1903, https://doi.org/10.1111/j.1365-3091.2008.00971.x.
Gardner, J.V., 2010, The West Mariana Ridge, western Pacific Ocean: Geomorphology and processes from new multibeam data: Geological Society of America Bulletin, v. 122, no. 9/10, p. 1378–1388, https://doi.org/10.1130/B30149.1.
Gill, J.B., Hiscott, R.N., and Vidal, P., 1994, Turbidite geochemistry and evolution of the Izu-Bonin arc and continents: Lithos, v. 33, no. 1–3, p. 135–168, https://doi.org/10.1016/0024-4937(94)90058-2.
Hamada, M., Iwamori, H., Brandl, P.A., Ushikubo, T., Shimizu, K., Ito, M., Li, H., and Savov, I.P., 2020, Temporal evolution of proto–Izu-Bonin-Mariana arc volcanism: Constraints from the statistical analysis of melt inclusion composition: Journal of Petrology, v. 61, egaa022, https://doi.org/10.1093/petrology/egaa022.
Harford, C.L., Pringle, M.S., Sparks, R.S.J., and Young, S.R., 2002, The volcanic evolution of Montserrat using $^{40}Ar/^{39}Ar$ geochronology, *in* Druitt, T.H., and Kokelaar, B.P., eds., The Eruption of Soufrière Hills Volcano, Montserrat, from 1995 to 1999: Geological Society [London] Memoir 21, p. 93–113, https://doi.org/10.1144/GSL.MEM.2002.021.01.05.
Hickey-Vargas, R., Yogodzinski, G., Ishizuka, O., McCarthy, A., Bizimis, M., Kusano, Y., Savov, I.P., and Arculus R., 2018, Origin of depleted basalts during subduction initiation and early development of the Izu-Bonin-Mariana Island arc: Evidence from IODP Expedition 351 Site U1438, Amami-Sankaku Basin: Geochimica et Cosmochimica Acta, v. 229, p. 85–111, https://doi.org/10.1016/j.gca.2018.03.007.
Hiscott, R.N., and Gill, J.B., 1992, Major and trace element geochemistry of Oligocene to Quaternary volcaniclastic sands and sandstones from the Izu–Bonin Arc, *in* Proceedings of the Ocean Drilling Program, Scientific Results: College Station, Texas, Government Printing Office, v. 125, p. 467–486.
Houghton, B.F., and Landis, C.A., 1989, Sedimentation and volcanism in a Permian arc-related basin, southern New Zealand: Bulletin of Volcanology, v. 51, p. 433–450, https://doi.org/10.1007/BF01078810.
Hussong, D.M., Uyeda, S., et al., 1981, Initial Reports of the Deep Sea Drilling Project, Volume 60: Washington, D.C., U.S. Government Printing Office.
Ishizuka, O., Taylor, R.N., Yuasa, M., and Ohara, Y., 2011, Making and breaking an island arc: A new perspective from the Oligocene Kyushu-Palau arc, Philippine Sea: Geochemistry Geophysics Geosystems, v. 12, Q05005, https://doi.org/10.1029/2010GC003440.
Ishizuka, O., Hickey-Vargas, R., Arculus, R.J., Yogodzinski, G.M., Savov, I.P., Kusano, Y., McCarthy, A., Brandl, P.A., and Sudo, M., 2018, Age of Izu-Bonin-Mariana arc basement: Earth and Planetary Science Letters, v. 481, p. 80–90, https://doi.org/10.1016/j.epsl.2017.10.023.
Ishizuka, O., Taylor, R.N., Umino, S., and Kanayama, K., 2020, Geochemical evolution of arc and slab following subduction initiation: A record from the Bonin Islands, Japan: Journal of Petrology, v. 61, no. 5, p. egaa050, https://doi.org/10.1093/petrology/egaa050.
Jobe, Z.R., Howes, N.C., Straub, K.M., Cai, D., Deng, H., Laugier, F.J., Pettinga, L.A., and Shumaker, L.E., 2020, Comparing aggradation, superelevation, and avulsion frequency of submarine and fluvial channels: Frontiers of Earth Science, v. 8, p. 53, https://doi.org/10.3389/feart.2020.00053.
Johnson, K., Waldman, R., and Marsaglia, K., 2017, Data report: Sedimentary columns with facies and bedding for units II–IV at IODP Site U1438, *in* Arculus, R.J., Ishizuka, O., Bogus, K., and the Expedition 351 Scientists, eds., Proceedings of the International Ocean Discovery Program (IODP), Volume 351: College Station, Texas, International Ocean Discovery Program, https://doi.org/10.14379/iodp.proc.351.201.2017.
Jutzeler, M., Manga, M., White, J.D.L., Talling, P.J., Proussevitch, A.A., Watt, S.F.L., Cassidy, M., Taylor, R.N., Le Friant, A., and Ishizuka, O., 2017, Submarine deposits from pumiceous pyroclastic density currents traveling over water: An outstanding example from offshore Montserrat (IODP 340): Geological Society of America Bulletin, v. 129, p. 392–414, https://doi.org/10.1130/B31448.1.
Kokelaar, P., and Romagnoli, C., 1995, Sector collapse, sedimentation and clast population evolution at an active island-arc volcano: Stromboli, Italy: Bulletin of Volcanology, v. 57, p. 240–262, https://doi.org/10.1007/BF00265424.
Kroenke, L., and Scott, R., et al., 1980, Initial Reports of the Deep Sea Drilling Project, Volume 59: Washington, D.C., U.S. Government Printing Office.
Laxton, K.A., 2016, Petrological and Geochemical Evolution of the Kyushu-Palau (Early IBM) Volcanic Arc, Western Pacific [M.Sc. thesis]: Leeds, UK, School of Earth and Environment, University of Leeds, 111 p.
Le Friant, A., Ishizuka, O., Stroncik, N.A., and the Expedition 340 Scientists, 2013, Proceedings of the International Ocean Discovery Program (IODP), Volume 340: Tokyo, Japan, Integrated Ocean Drilling Program Management International, http://publications.iodp.org/proceedings/340/340toc.htm.
Le Friant, A., Ishizuka, O., Boudon, G., Palmer, M.R., Talling, P.J., Villemant, B., Adachi, T., Aljahdali, M., Breitkreuz, C., Brunet, M., Caron, B., Coussens, M., Deplus, C., Endo, D., Feuillet, N., Fraas, A.J., Fujinawa, A., Hart, M.B., Hatfield, R.G., Hornbach, M., Jutzeler, M., Kataoka, K.S., Komorowski, J.-C., Lebas, E., Lafuerza, S., Maeno, F., Manga, M., Martınez-Colon, M., McCanta, M., Morgan, S., Saito, T., Slagle, A., Sparks, S., Stinton, A., Stroncik, N., Subramanyam, K.S.V., Tamura, Y., Trofimovs, J., Voight, B., Wall-Palmer, D., Wang, F., and Watt, S.F.L., 2015, Submarine record of volcanic island construction and collapse in the Lesser Antilles arc: First scientific drilling of submarine volcanic island landslides by IODP Expedition 340: Geochemistry Geophysics Geosystems, v. 16, p. 420–442, https://doi.org/10.1002/2014GC005652.
Lowe, D., 1982, Sediment gravity flows: II: Depositional models with special reference to the deposits of high-density turbidity currents: Journal of Sedimentary Petrology, v. 52, p. 279–297.
Marsaglia, K.M., 1992, Petrography and provenance 436 of volcaniclastic sands recovered from the Izu-Bonin arc, Leg 126: Proceedings of the Ocean Drilling Program, Scientific Results, v. 126, p. 139–154, http://www-odp.tamu.edu/publications/126_SR/126TOC.HTM.
Marsaglia, K.M., 1995, Interarc and backarc basins, *in* Busby, C., and Ingersoll, R.V., eds., Tectonics of Sedimentary Basins: Oxford, Blackwell, p. 299–329.
Marsaglia, K.M., and Devaney, K.A., 1995, Tectonic and magmatic controls on backarc basin sedimentation: The Mariana region reexamined, *in* Taylor, B., ed., Backarc Basins: Tectonics and Magmatism: New York, Plenum, p. 497–520, https://doi.org/10.1007/978-1-4615-1843-3_14.
Marsaglia, K.M., and Tazaki, K., 1992, Diagenetic trends in Leg 126 sandstones, *in* Proceedings of the Ocean Drilling Program, Scientific Results, v. 126, p. 125–138.
Marsaglia, K.M., Barone, M., Critelli, S., and Busby, C., 2016, Petrography of volcaniclastic rocks in intra-arc volcano-bounded to fault-bounded basins of the Lower Cretaceous Alisitos oceanic arc, Baja California, Mexico: Sedimentary Geology, v. 336, p. 138–146, https://doi.org/10.1016/j.sedgeo.2015.11.008.
Morrone, C., DeRosa, R., Le Pera, E., and Marsaglia, K.M., 2017, Provenance of volcaniclastic beach sand in a magmatic arc setting: An example from Lipari island beaches (Aeolian Archipelago, Tyrrhenian Sea): Geological Magazine, v. 154, p. 804–828, https://doi.org/10.1017/S001675681600042X.
Mutti, E., and Normark, W.R., 1987, Comparing examples of modern and ancient turbidite systems: Problems and concepts, *in* Leggett, J.K., and Zuffa, G.G., eds., Marine Clastic Sedimentology: London, Graham & Trotman, p. 1–38, https://doi.org/10.1007/978-94-009-3241-8_1.
Mutti, E., and Ricci Lucchi, F., 1972, Le torbiditi dell'Appennino settentrionale; introduzione all' analisi di facies: Bollettino della Società Geologica Italiana, v. 11, p. 161–199.

Nichols, A.R.L., Wysoczanski, R.J., Tani, K., Tamura, Y., Baker, J.A., and Tatsumi, Y., 2012, Melt inclusions reveal geochemical cross-arc variations and diversity within magma chambers feeding the Higashi-Izu Monogenetic Volcano Field, Izu Peninsula, Japan: Geochemistry, Geophysics, Geosystems, v. 13, https://doi.org/10.1029/2012GC004222.

Pavlis, T.L., Amato, J.M., Trop, J.M., Tidgway, K.D., Roeske, S.M., and Gehrels, G.E., 2019, Subduction polarity in ancient arcs: A call to integrate geology and geophysics to decipher the Mesozoic tectonic history of the northern Cordillera of North America: GSA Today, v. 29, no. 11, p. 4–10, https://doi.org/10.1130/GSATG402A.1.

Pettinga, L., Jobe, Z., Shumaker, L., and Howes, N., 2018, Morphometric scaling relationships in submarine channel-lobe systems: Geology, v. 46, p. 819–822, https://doi.org/10.1130/G45142.1.

Picard, M., Schneider, J.-L., and Boudon, G., 2006, Contrasting sedimentary processes along a convergent margin: The Lesser Antilles arc system: Geo-Marine Letters, v. 26, p. 397–410, https://doi.org/10.1007/s00367-006-0046-y.

Pickering, K., Stow, D., Watson, M., and Hiscott, R., 1986, Deep-water facies, processes and models: A review and classification scheme for modern and ancient sediments: Earth-Science Reviews, v. 23, p. 75–174, https://doi.org/10.1016/0012-8252(86)90001-2.

Pickering, K.T., and Hiscott, R.N., 2015, Deep Marine Systems: Processes, Deposits, Environments, Tectonics and Sedimentation: New York, Wiley-Blackwell, 776 p.

Pope, E.L., Jutzler, M., Cartigny, M., Shreeve, J., Talling, P., Wright, I.C., and Wyxoczanski, R.J., 2018, Origin of spectacular fields of submarine sediment waves around volcanic islands: Earth and Planetary Science Letters, v. 493, p. 12–24, https://doi.org/10.1016/j.epsl.2018.04.020.

Prélat, A., Hodgson, D.M., and Flint, S.S., 2009, Evolution, architecture and hierarchy of distributary deep-water deposits: A high-resolution outcrop investigation from the Permian Karoo Basin, South Africa: Sedimentology, v. 56, 2132–2154, https://doi.org/10.1111/j.1365-3091.2009.01073.x.

Prueher, L.M., and Rea, D.K., 2001, Tephrochronology of the Kamchatka-Kurile and Aleutian arcs; evidence for volcanic episodicity: Journal of Volcanology and Geothermal Research, v. 106, p. 67–84, https://doi.org/10.1016/S0377-0273(00)00266-3.

Pyles, D.R., Fleming, A., and Anderson, D.S., 2019, Hierarchical organization and spatial variations of lobes in distributive submarine fans: Outcrop study of the Point Loma Formation, California, USA, *in* Marsaglia, K.M., Schwalbach, J., and Behl, R., eds., From the Mountains to the Abyss: The California Borderland as an Archive of Southern California Geologic Evolution: Society of Sedimentary Geology (SEPM) Special Publication 110, p. 135–157, https://doi.org/10.2110/sepmsp.110.09.

Robertson, A., and Degnan, P., 1994, The Dras arc complex: Lithofacies and reconstruction of a Late Cretaceous oceanic volcanic arc in the Indus suture zone, Ladakh Himalaya: Sedimentary Geology, v. 92, p. 117–145, https://doi.org/10.1016/0037-0738(94)90057-4.

Robertson, A.H.F., and Collins, A.S., 2002, Shyok suture zone, N Pakistan: Late Mesozoic–Tertiary evolution of a critical suture separating the oceanic Ladakh arc from the Asian continental margin: Journal of Asian Earth Sciences, v. 20, p. 309–351, https://doi.org/10.1016/S1367-9120(01)00041-4.

Robertson, A.H.F., Kutterolf, S., Avery, A., Baxter, A.T., Petronotis, K., Acton, G.D., Carvallo, C., and Schindlbeck, J.C., 2018, Depositional setting, provenance, and tectonic-volcanic setting of Eocene–Recent deep-sea sediments of the oceanic Izu-Bonin forearc, northwest Pacific (IODP Expedition 352): International Geology Review, v. 60, no. 15, p. 1816–1854, https://doi.org/10.1080/00206814.2017.1393634.

Romagnoli, C., Casalbore, D., Chiocci, F.L., and Bosman, A., 2009, Offshore evidence of large-scale lateral collapses on the eastern flank of Stromboli, Italy, due to structurally-controlled, bilateral flank instability: Marine Geology, v. 262, p. 1–13, https://doi.org/10.1016/j.margeo.2009.02.004.

Ryan, W.B., Carbotte, S.M., Coplan, J.O., O'Hara, S., Melkonian, A., Arko, R., Weissel, R.A., Ferrini, V., Goodwillie, A., Nitsche, F., and Bonczkowski, J., 2009, Global multi-resolution topography synthesis: Geochemistry, Geophysics, Geosystems, v. 10, https://doi.org/10.1029/2008GC002332.

Salisbury, M.H., Shinohara, M., Richter, C., et al., 2002, Proceedings Ocean Drilling Program, Initial Reports, Volume 195: College Station, Texas, Ocean Drilling Program, https://doi.org/10.2973/odp.proc.ir.195.2002.

Savov, I.P., Hickey-Vargas, R., D'Antonio, M., Ryan, J.G., and Spadea, P., 2006, Petrology and geochemistry of West Philippine Basin basalts and early Palau-Kyushu arc volcanic clasts from ODP Leg 195, Site 1201D: Implications for the early history of the Izu-Bonin-Mariana arc: Journal of Petrology, v. 47, p. 277–299, https://doi.org/10.1093/petrology/egi075.

Schiffman, P., Spero, H.J., Southard, R.J., and Swanson, D.A., 2000, Controls on palagonitization versus pedogenic weathering of basaltic tephra: Evidence from the consolidation and geochemistry of the Keanakako'i Ash Member, Kilauea Volcano: Geochemistry Geophysics Geosystems, v. 1, 1040, https://doi.org/10.1029/2000GC000068.

Shipboard Scientific Party, 2002, Site 1201, Ocean Drilling Program, Initial Reports, Volume 195: College Station, Texas, Ocean Drilling Program, https://doi.org/10.2973/odp.proc.ir.195.104.2002.

Spasojevic, S., and Gurnis, M., 2012, Sea level and vertical motion of continents from dynamic earth models since the Late Cretaceous: American Association of Petroleum Geologists Bulletin, v. 96, p. 2037–2064, https://doi.org/10.1306/03261211121.

Stow, D.A.V., and Shanmugam, G., 1980, Sequence of structures in fine-grained turbidites: Comparison of recent deep-sea and ancient flysch sediments: Sedimentary Geology, v. 25, p. 23–42, https://doi.org/10.1016/0037-0738(80)90052-4.

Straub, S.M., Woodhead, J., and Arculus, R.J., 2015, Temporal evolution of the Mariana arc: Mantle wedge and subducted slab controls revealed with a tephra perspective: Journal of Petrology, v. 56, no. 2, p. 409–439, https://doi.org/10.1093/petrology/egv005.

Sweet, M.L., Gaillot, G.T., Jouet, G., Rittenour, T.M., Toucanne, S., Marsset, T., and Blum, M.D., 2020, Sediment routing from shelf to basin floor in the Quaternary Golo system of eastern Corsica, France, western Mediterranean Sea: Geological Society of America Bulletin, v. 132, p. 1217–1234, https://doi.org/10.1130/B35181.1.

Taylor, B., Fujioka, K., and Shipboard Scientific Party, 1990, Proceedings of the Ocean Drilling Program, Initial Reports, Volume 126: College Station, Texas, Ocean Drilling Program, https://doi.org/10.2973/odp.proc.ir.126.1990.

Trofimovs, J., Sparks, S.J., and Talling, P.J., 2008, Anatomy of a submarine pyroclastic flow and associated turbidity current: July 2003 dome collapse, Soufrière Hills volcano, Montserrat, West Indies: Sedimentology, v. 55, p. 617–634, https://doi.org/10.1111/j.1365-3091.2007.00914.x.

Waldman, R., Marsaglia, K.M., Hicky-Varga, R., Ishizuka, O., Johnson, K.E., McArthy, A., Yogodzinski, G., Samajpati, E., Li, H., Laxton, K., Savov, I.P., Meffre, S., Arculus, R.J., Bandini, A.N., Barth, A., Bogus, K., Brandl, P.A., Gurnis, M., and Jiang, R., 2021, Sedimentary and volcanic record of the nascent Izu-Bonin-Mariana arc from IODP Site U1438: Geological Society of America Bulletin, https://doi.org/10.1130/B35612.1 (in press).

Watt, S.F.L., Talling, P.J., Vardy, M.E., Masson, D.G., Henstock, T.J., Hühnerbach, V., Minshull, T.A., Urlaub, M., Lebas, E., Le Friant, A., Berndt, C., Crutchley, G.J., and Karstens, J., 2012, Widespread and progressive seafloor-sediment failure following volcanic debris avalanche emplacement: Landslide dynamics and timing offshore Montserrat, Lesser Antilles: Marine Geology, v. 323–325, p. 69–94, https://doi.org/10.1016/j.margeo.2012.08.002.

Watts, A.B., Peirce, C., Grevemeyer, I., Paulatto, M., Stratford, W., Bassett, D., Hunter, J.A., Kalnins, L.M., and de Ronde, C.E.J., 2012, Rapid rates of growth and collapse of Monowai submarine volcano in the Kermadec arc: Nature Geoscience, v. 5, p. 510–515, https://doi.org/10.1038/ngeo1473.

Wilson, C.J.N., Houghton, B.F., McWilliams, M.O., Lanphere, M.A., Weaver, S.D., and Briggs, R.M., 1995, Volcanic and structural evolution of Taupo volcanic zone, New Zealand: A review: Journal of Volcanology and Geothermal Research, v. 68, p. 1–28, https://doi.org/10.1016/0377-0273(95)00006-G.

Wombacher, F., and Münker, C., 2000, Pb, Nd, and Sr isotopes and REE systematics of Cambrian sediments from New Zealand: Implications for the reconstruction of the early Paleozoic Gondwana margin along Australia and Antarctica: The Journal of Geology, v. 108, p. 663–686, https://doi.org/10.1086/317950.

Yogodzinski, G.M., Bizimis, M., Hickey-Vargas, R., McCarthy, A., Hocking, B.D., Savov, I.P., Ishizuka, O., and Arculus, R., 2018, Implications of Eocene-age Philippine Sea and forearc basalts for initiation and early history of the Izu-Bonin-Mariana arc: Geochimica et Cosmochimica Acta, v. 228, p. 136–156, https://doi.org/10.1016/j.gca.2018.02.047.